Bioactive Materials 6 (2021) 1436–1451

Contents lists available at ScienceDirect

Bioactive Materials

journal homepage: www.sciencedirect.com/journal/bioactive-materials

The influence of Ca and Cu additions on the microstructure, mechanical and degradation properties of Zn–Ca–Cu alloys for absorbable wound closure device applications

Nan Yang [a], Nagasivamuni Balasubramani [a], Jeffrey Venezuela [a], Sharifah Almathami [a], Cuie Wen [b], Matthew Dargusch [a,*]

[a] Queensland Centre for Advanced Materials Processing and Manufacturing (AMPAM), School of Mechanical and Mining Engineering, Advanced Engineering Building, Bld 49, The University of Queensland, Staff House Rd, St Lucia, QLD, 4072, Australia
[b] School of Engineering, RMIT University, Melbourne, Victoria, 3001, Australia

ARTICLE INFO

Keywords:
Zn-Ca-Cu alloy
Solidification
Mechanical properties
In vitro degradation

ABSTRACT

Novel ternary Zn–Ca–Cu alloys were studied for the development of absorbable wound closure device material due to Ca and Cu's therapeutic values to wound healing. The influence of Ca and Cu on the microstructure, mechanical and degradation properties of Zn were investigated in the as-cast state to establish the fundamental understanding on the Zn–Ca–Cu alloy system. The microstructure of Zn-0.5Ca-0.5Cu, Zn-1.0Ca-0.5Cu, and Zn0.5Ca-1.0Cu is composed of intermetallic phase $CaZn_{13}$ distributed within the Zn–Cu solid solution. The presence of $CaZn_{13}$ phase and Cu as solute within the Zn matrix, on the one hand, exhibited a synergistic effect on the grain refinement of Zn, reducing the grain size of pure Zn by 96%; on the other hand, improved the mechanical properties of the ternary alloys through solid solution strengthening, second phase strengthening, and grain refinement. The degradation properties of Zn–Ca–Cu alloys are primarily influenced by the micro-galvanic corrosion between Zn–Cu matrix and $CaZn_{13}$ phase, where the 0.5% and 1.0% Ca addition increased the corrosion rate of Zn from 11.5 μm/y to 19.8 μm/y and 29.6 μm/y during 4 weeks immersion test.

1. Introduction

Driven by the increasing number of operations, incidences, and chronic wound injuries globally, the wound closure device market has undergone significant development in terms of the techniques and the materials used [1]. Both absorbable (e.g. polyglycolic acid, polylactic acid) and non-absorbable materials (e.g. stainless steel, titanium) have been used in different devices that enable the closing and eventual healing of various types of wounds [2].

Absorbable wound closure materials, which are mostly polymer-based, have won favour in current clinical practices, because these materials eliminate the need for secondary surgery for removal. However, the limited tensile strength of polymers has limited their applicability to the closure of low-tension wounds. Therefore, such limitation necessitates the development of strong, absorbable wound closure materials.

In the recent decade, biodegradable metals (BMs), namely magnesium (Mg), zinc (Zn), and iron (Fe) and their alloys have been extensively studied as promising candidates for absorbable biomedical implant applications [3–5]. Current studies on BMs are mostly focusing on stents and orthopaedic implant applications [6–8]. In 2015, Seitz et al. [9] published a review on the suitability of biodegradable metals (BMs), namely, Mg, Zn, Fe and their alloys as potential absorbable suture materials for wound closure applications. They proposed that BMs are promising substitutes to the traditional polymeric-based suture materials due to several advantages. Firstly, BMs possess a wide range of excellent mechanical properties; for example, Fe intrinsically possesses high strength which is ideal for load-bearing applications, while Mg and Zn, can be easily strengthened by microstructure manipulation. Secondly, BMs have good biocompatibility as these naturally exist in human body, and both the metal and its ions and even some of the biodegradation products participate in numerous human physiological functions [10].

For wound closure applications, Mg and Fe offer some advantages such as excellent biocompatibility and outstanding mechanical properties, respectively [11–13]. However, Mg possesses the highest

* Corresponding author.
E-mail address: m.dargusch@uq.edu.au (M. Dargusch).

https://doi.org/10.1016/j.bioactmat.2020.10.015
Received 4 September 2020; Received in revised form 21 October 2020; Accepted 21 October 2020

degradation rate among all BMs, which is commonly associated with short strength retention period that appears insufficient for wound support [9]. In addition, Mg degradation is typically associated with hydrogen gas generation [14]. Fe has some issues due to its low corrosion rate, which often triggers tissue responses similar to that of permanent implants, and the generation of bulky insoluble degradation product [15].

Recently, Venezuela et al. [16] critically assessed the prospect of Zn in wound closure application. They suggested that Zn may become a promising candidate not only as absorbable sutures, but also as staples, surgical tacks, and other advanced wound closure devices. Zn biodegradation is gas-free and associated with minimum degradation product generation; therefore, it is believed to pose minimal adverse impact on the wound environment. Another advantage that favours Zn for wound closure application is its moderate biodegradation rate compare to Fe and Mg, which implies a prolonged strength retention period that coincides with that of tissue healing time as sternal suture.

However, pure Zn possesses limited mechanical properties, with yield strength (*YS*) and ultimate tensile strength (*UTS*) of 30 MPa and 50 MPa, respectively [17], which are often insufficient for biomedical applications. Even after hot working, the *UTS* of Zn wire is still far below the mechanical properties required of some traditional sutures [9,18].

Alloying is an effective method to improve the mechanical properties of Zn. Currently, there are over thirty types of Zn-based binary, ternary and quaternary alloy systems being studied for biomedical applications [19–21]. These alloys were derived from the combination of thirteen alloying elements, including calcium (Ca), magnesium (Mg), iron (Fe), copper (Cu), manganese (Mn), strontium (Sr), aluminium (Al), zirconium (Zr), lithium (Li), germanium (Ge), silver (Ag), titanium (Ti), and bismuth (Bi). Although all of these elements have demonstrated different levels of strengthening effect on Zn, the biocompatibility of these alloying elements require further consideration. Biocompatibility is an important consideration in candidate materials for biodegradable medical devices. Unlike traditional permanent metallic implants, which uses materials that are biologically inert, biodegradable implants require both the material and its degradation by-products to be completely biocompatible to the host. In addition, Zheng et al. [10] proposed to go beyond the criteria of 'non-toxicity', as it is also important to fully exploit the bio-functions of the degradation products of BMs. Liu et al. [22] considered the biodegradation of BMs as a 'bioactive' process, which could potentially benefit the healing of affected tissues. Dennis et al. [23] provided specific recommendation to the development of next generation wound closure materials. They proposed that novel wound closure materials should not just provide the "physical closure of wounds", but also "promote wound healing through the addition of features such as antimicrobial agents, bioactive molecules and drugs". Evidently, it would be a great advantage if the wound closure material itself could also promote the wound healing process through the release of 'bio-active' metal ions during the biodegradation process.

Zn is an essential trace element in the human body, and it plays a critical role in homeostasis, immune function, oxidative stress, cell apoptosis, and aging in humans [24]. During wound healing, Zn^{2+} plays an important role in regulating the cellular activities that are essential for the haemostasis, inflammation, proliferation, and remodelling of wound site [25]. In addition, the supplement of Zn, either by oral intake or topical application, could shorten the time for wound healing [26,27]. Moreover, the degradation products of Zn, including $Zn(OH)_2$ and ZnO, possess anti-inflammatory effect [28] and are commonly used as anti-inflammatory agents in wound management [25,29].

Ca and Cu based compounds are also widely used in wound management to increase promote the healing tissue process. Topical Ca^{2+} supplement, either though intravenous injection or wound dressing, could improve the wound strength, decrease the wound size and shorten the time for wound healing [29,30]. Similarly, Cu-based wound dressings and Cu-containing biodegradable implants have also demonstrated effective antibacterial effect to the microbials that are related to post-operation surgical site infection [31–33].

Given the therapeutic values of Zn, Ca and Cu to wound healing, a Zn–Ca–Cu alloy appears to be a promising candidate for the fabrication of absorbable wound closure devices. However, research on such an alloy system has not been reported, and the current understanding is limited to either Zn–Ca or Zn–Cu binary alloys [17,31,33–37]. Recent investigations on Zn–Ca alloys have indicated that Ca can significantly increase the mechanical properties and degradation rate of Zn through the formation of $CaZn_{13}$ [17,37]. Cu has also demonstrated great promise as an alloying element in biodegradable Zn alloys. For example, Cu is well-cited for improving the tensile properties, hardness, wear resistance and creep resistance of Zn alloys [34]. Previous studies on binary Zn–Cu alloys have reported that Cu significantly improved the tensile properties of Zn through precipitation strengthening and solid solution strengthening. In addition, the strengthening of Zn–Cu alloys occurs with minimal compromise of ductility [31,33,35]. Therefore, Cu is considered as an ideal alloying element for Zn, inducing a balance of strengthening and toughening effect [36]. However, the influence of Cu additions on the corrosion resistance of Zn is still debatable. Different studies have reported that Cu either increase [31], decrease [35], or negligibly affect [33] the corrosion resistance of Zn. Therefore, a general understanding of the influence of Ca and Cu additions on the mechanical and corrosion characteristics of Zn would be necessary prior to the fabrication of Zn–Ca–Cu-based wound closure devices.

The current investigation is focused on developing and understanding the properties of a novel Zn–Ca–Cu ternary alloy. In order to achieve this, five alloy systems, namely, Zn-0.5Cu, Zn-0.5Ca, Zn-0.5Ca-0.5Cu, Zn-0.5Ca-1.0Cu and Zn-1.0Ca-0.5Cu were fabricated and studied for microstructure, mechanical and in-vitro corrosion in the as-cast state. For each investigated alloy, the total alloying element content was limited to less than 1.5 wt% composition. This alloy composition value was recommended for biodegradable Zn as alloys with composition beyond this limiting value often tends to exhibit undesirable properties [19]. Several attributes of the as-cast structure, such as grain size refinement and evolution of intermetallic phases were related to the alloy's strengthening and corrosion behaviour. The evaluation of these fundamental properties of the alloys are considered to be important first steps for the prospective development of Zn-based biodegradable wound closure devices.

2. Methodology

2.1. Material preparation

Alloys of Zn with nominal compositions of Zn-0.5Cu, Zn-0.5Ca, Zn-0.5Ca-0.5Cu, Zn-1.0Ca-0.5Cu, Zn-1.0Cu-0.5Ca were prepared using high purity zinc ingot (99.995 wt %), pure copper (99.9 wt%), Zn-5 wt. % Ca, and Zn-5 wt.% Cu master alloys. Approximately 3 kg of pure Zn and Zn–Cu alloys were melted in an induction melting furnace at an operating power of 8 kW. Melting of Ca containing Zn alloys are conducted in an electric resistance furnace under the protective gas atmosphere (1 vol% SF_6 and CO_2). Pure Zn ingot was melted at 600 °C and the required quantities of Zn–Ca and Zn–Cu master alloys are added to the melt. The melt temperature was increased to 720 °C for the addition of Zn–Ca and Zn–Ca–Cu ternary alloys for the dissolution of Ca. The melt was held at 720 °C for 15–20 min, stirred every 5 min to ensure the complete dissolution of Ca and then poured into a steel mould preheated at 200 °C. Fig. 1 shows the diagram of the mould and the casting indicating the sampling locations for microstructure, mechanical properties and corrosion. The rectangular section (130 mm in length, 70 mm in height and 20 mm in thickness) sliced from the bottom portion of the casting was used for mechanical and corrosion testing. Cylindrical samples of Ø15 × 3 mm, Ø15 × 6 mm, and Ø6 x 12 mm were machined for immersion test, potentiodynamic polarization test and uniaxial compression test, respectively. Tensile specimens were prepared

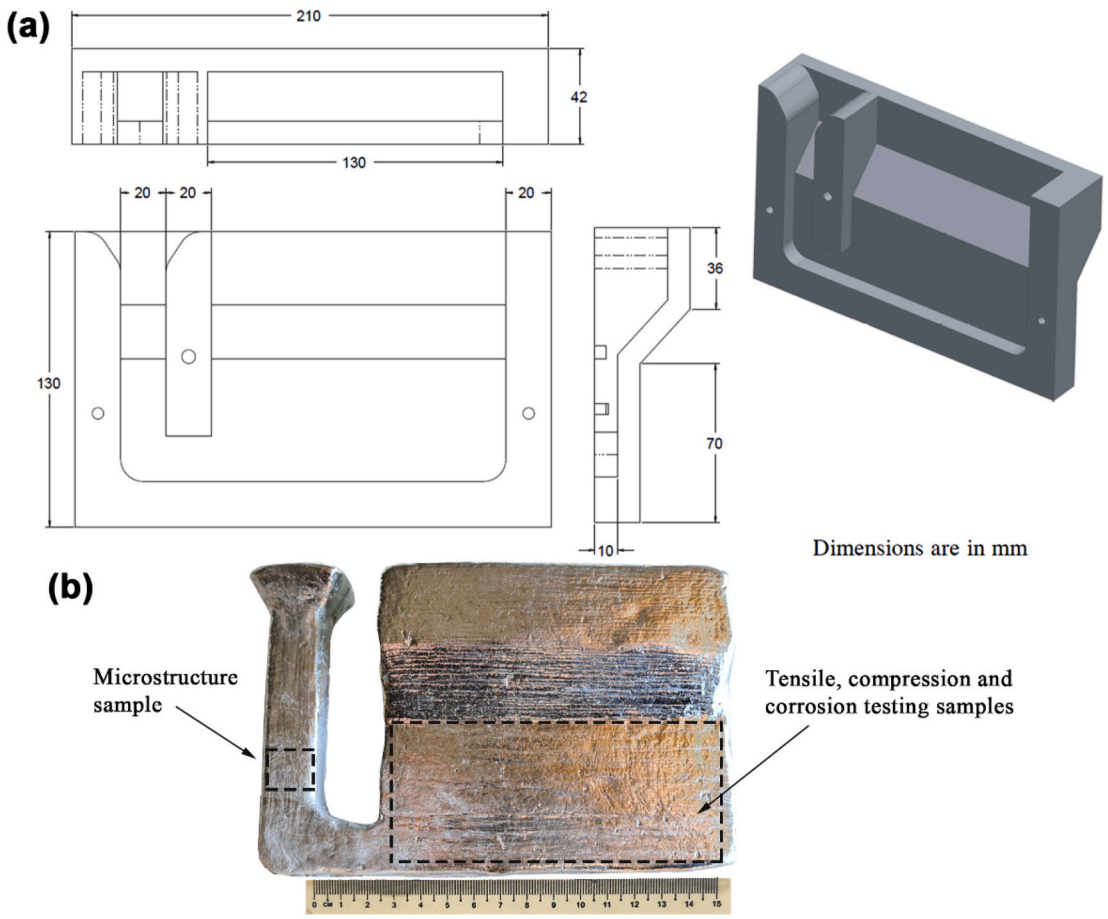

Fig. 1. (a) A symmetrical section of the CAD model and the dimensions of the mould and (b) cast pure Zn marked with the sampling locations of microstructure, mechanical properties and corrosion analysis.

following ASTM E8 [38].

2.2. Microstructural characterization and compositional analysis

Specimens with approximate dimensions of 10x10 × 10 mm^3 were cut for microstructure characterization, then cold-mounted in epoxy resin for polishing. The samples were ground using SiC abrasive papers from 600 to 4000 grit, and then final polished using diamond and colloidal silica suspension. The polished samples were chemically etched using a solution of 15 mL H_2SO_4 and 1 mL HF in water for 15 s to reveal the microstructure. Microstructure images were acquired using Leica Polyvar optical microscope at different magnifications under polarised mode. Grain size measurements and intermetallic phase area was calculated using an image analysis software. Hitachi TM3030, table-top scanning electron microscope (SEM, containing X-ray energy dispersive spectrometry (EDS)) was used to characterize the intermetallic phases. Grain size measurement and the relative amount of the second phase were evaluated using ASTM E1382-97 [39] and ASTM E1245-03 [40] with the help of an image analysis software. Bruker D8 Advance MKII X-ray diffraction equipment was used to characterize the phases formed at an accelerating voltage of 40 kV, at 40 mA (Cu Kα radiation) and a scan rate of 2°/min.

2.3. Mechanical test

Uniaxial tensile and compression tests were performed using a universal test machine (UTM, Instron 5584, USA) at room temperature in accordance with ASTM E8/E8M and ASTM E9-19 [38,41]. Tensile test and compression test were conducted at a strain rate of 10^{-3}/s and10^{-1}/s, respectively. Five replicates were conducted for each alloy type. The tensile yield strength (*YS*), ultimate tensile strength (*UTS*), elongation (*E*), compressive yield strength (*CYS*), ultimate compressive strength (*UCS*) and compressive elastic modulus (E_c) were obtained from the relevant Instron software.

Vickers hardness test was conducted according to ASTM E92-17 [42]. At least ten points from each specimen were randomly selected as test locations. The test was performed at room temperature, at an applied load of 1 kg and a loading duration of 10 s.

2.4. Immersion test

The immersion test on the as-cast pure Zn and Zn alloy buttons (Ø16 × 3 mm) were conducted in Hank's solution (HBSS, Sigma-Aldrich H1387) at 37 °C according to ASTM F3263-18a [43]. The solution volume to sample surface area ratio was controlled at 0.2 mL/mm^2. The specimens were collected at the 4-week and 8-week immersion periods. The specimens were rinsed in ethanol, then dried with compressed air for corrosion morphology characterization (SEM). The corrosion products of the specimens were removed by chromic oxide solution (200 g/L Cr_2O_3) at 40 °C for 5 min. The acid cleaning was conducted multiple times until the weight of the samples was stabilized.

The corrosion rate of the test specimen was calculated by equation:

$$CR = KW/At\rho \quad (1)$$

where *K* is a constant; *W* is the weight loss of the specimen in g; *A*, *t*, ρ are the surface area (cm^2), time of exposure (h), and the density of the specimen (g/cm^3), respectively.

2.5. Polarization measurement

Potentiodynamic polarization were conducted on the specimens in Hank's solution (HBSS, Sigma-Aldrich H1387) using a potentiostat (PARSTAT® 2273). The temperature and the PH of each test were kept at 37 ± 0.5 °C and 7.4 ± 0.2, respectively. A three-electrode electrochemical cell was used for the polarization measurement, including a counter electrode (10*15*0.2 mm platinum plate), a reference electrode (saturated calomel electrode, SCE), and the Zn alloy as the working electrode. The specimen for electrochemical measurement was polished with 1200 grit SiC paper, and loaded in a sample holder which exposes a 1.0 cm^2 sample surface area to the test fluid.

For each electrochemical measurement, the open circuit potential (OCP) was monitored for 3600 s, followed by electrochemical impedance spectroscopy (EIS) and potentiodynamic polarization test. The EIS measurement was conducted using a 10 mV sinusoidal perturbating signal at the frequency range from 100 KHz to 100 mHz. The analysis of EIS data is performed using an electrochemical analysis software (ZView). The potentiodynamic polarization measurement was carried out at the scan rate of 0.166 mV/s, in the potential range of −250 mV vs. OCP and completed at +250 mV vs. OCP. Three repeatable measurements were taken from each sample group. The corrosion current density (i_{corr}) was obtained through Tafel extrapolation as described in ASTM G102-89 [44] using electrochemical analysis software (CView). The corrosion rate during electrochemical measurement was calculated according to Faraday's law:

$$CR = KEi_{corr}/\rho \quad (2)$$

where CR is the corrosion rate in mm/yr, K is a constant equal to $3.27x10^3$, ρ is the density of the specimen, and E is the equivalent weight of the alloy.

3. Results

3.1. Microstructure characterization

Fig. 2 shows the microstructure of the binary and ternary Zn–Ca–Cu alloys. High purity Zn solidifies as large columnar grains that extend from the mould wall and terminate at the centre of the mould with an average size of 3.8 ± 1.1 mm. With a small addition of Cu, the Zn-0.5Cu alloys also exhibits columnar grain structure, however, the lateral growth of the dendrites is limited and finer columnar grains are observed (Fig. 2 - b). Addition of 0.5Ca in Zn-0.5Ca alloy produces better grain refinement than Cu additions to Zn-0.5Cu alloy as shown in Fig. 2 - c. Fine elongated grains together with fine equiaxed grains are present in the microstructure.

Generally, all the ternary alloys showed significant refinement than the binary alloys, with typical grain sizes being less than 150 μm (Fig. 2 – d, e, f). This is observed from Fig. 2b–f, where the columnar grains in the centre of the sample becomes fully equiaxed, although few fine elongated grains are also present near the mould wall regions. Interestingly, the ternary alloy with the higher Cu concentration, Zn-1.0Cu-0.5Ca (Fig. 2 - f), possesses a finer grain structure compared to the alloy with the higher Ca content, Zn-0.5Cu-1.0Ca alloy (Fig. 2 - e).

Fig. 3 – a, b shows the bright field optical microstructure images of the binary Zn-0.5Cu and Zn-0.5Ca alloy. According to the binary phase diagram of Zn–Cu alloys, the peritectic transition occurs for Cu concentrations above 1.7 wt% and Cu has a solid solubility limit of 2.75 wt % at 425 °C [33,35]. Therefore, 0.5 wt% addition of Cu (within the solubility limit of Cu of hypo-peritectic composition) does not show any intermetallic phases and appears similar to the pure Zn microstructure. Precipitation of the $CaZn_{13}$ phase was observed for all Ca-containing alloys. i.e. Zn-0.5Ca, Zn-0.5Ca-0.5Cu, Zn-0.5Ca-1.0Cu and Zn-1.0Ca-0.5Cu. Unlike Cu, Ca does not have appreciable solid solubility in Zn [45], and the precipitation of $CaZn_{13}$ is expected for all mixtures having Ca [17,37]. In the case of 0.5 and 1.0 wt% Ca added to binary and ternary Zn–Ca–Cu alloys, $CaZn_{13}$ nucleates at temperatures over 600 °C followed by the nucleation of η-Zn grains at 420 °C.

Fig. 3 – c, d, e, f show the BSD images of the Ca-containing binary and ternary alloys. These images reveal that the intermetallic phases are present within the matrix and grain boundaries. As observed from Fig. 3 – c, d, e, f, the increase in Ca from 0.5 wt% to 1.0 wt% promoted the growth of intermetallic dendrites, with some $CaZn_{13}$ dendrites extending to several millimetres in length that are observed throughout the sample. Ca addition at 1.0 wt% shows the massive precipitation of $CaZn_{13}$ dendrites (Fig. 3 - e). It is interesting to note that the increased addition of Cu to Zn-0.5Ca alloy in Zn-0.5Ca-0.5Cu alloy (Fig. 3 - d) and Zn-0.5Ca-1.0Cu alloy (Fig. 3 - f) also increases the size of the $CaZn_{13}$ dendrites. The remelted fragments of both primary and secondary $CaZn_{13}$ dendrites are dispersed throughout the microstructure. The area of fragmented $CaZn_{13}$ dendrites in the microstructure of Ca containing binary and ternary alloys are measured and the distribution is shown in Fig. 3 - g. The total area of the field of interest (A_t) and the area of the detected feature (A_i, $CaZn_{13}$ dendrites in this case) are calculated from various fields of the microstructure images. The area fraction of the intermetallic phases (A_A) present in the field of view is obtained by A_i/A_t for individual remelted fragments of $CaZn_{13}$ dendrites in the microstructure. Remelted primary and secondary dendrites that are separated

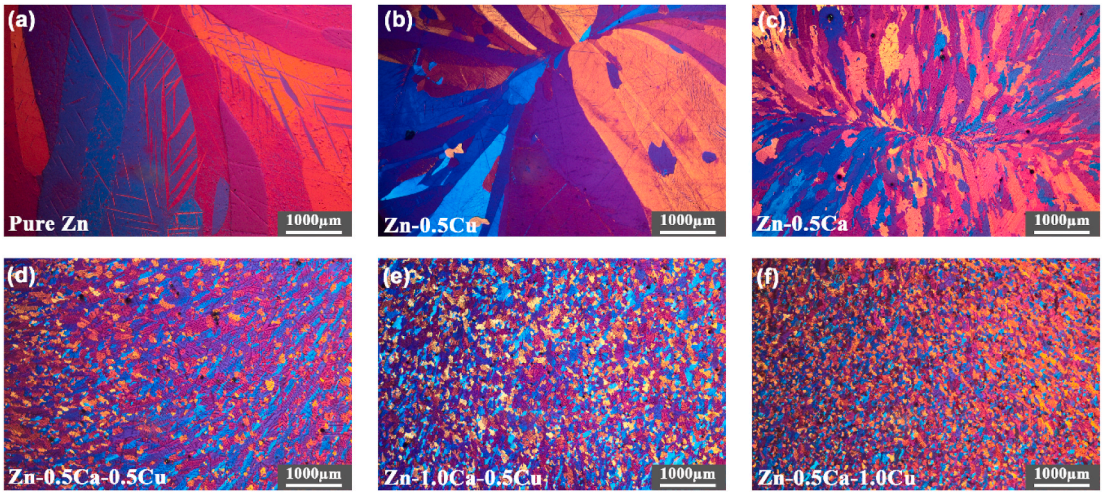

Fig. 2. Polarised microstructure images showing the grain refinement of (a) pure Zn, (b) Zn-0.5Cu, (c) Zn-0.5Ca, (d) Zn-0.5Cu-0.5Ca, (e) Zn-1.0Ca-0.5Cu and (f) Zn-0.5Ca-1.0Cu alloy.

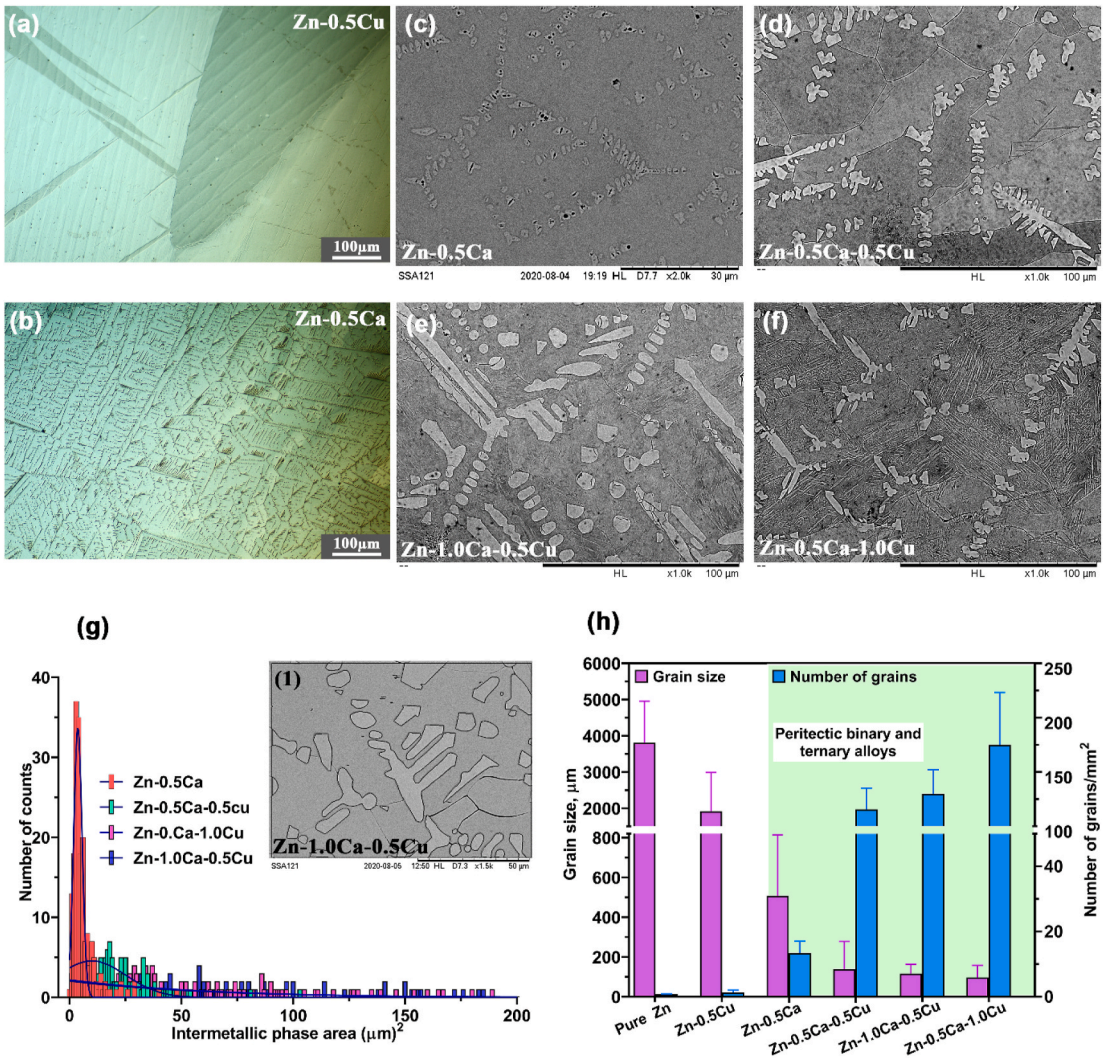

Fig. 3. Bright field optical microstructure images of (a) Zn-0.5Cu and (b) Zn-0.5Ca binary alloys. BSD images of (c) Zn-0.5Ca, (d) Zn-0.5Cu-0.5Ca, (e) Zn-1.0Ca-0.5Cu and (f) Zn-0.5Ca-1.0Cu alloys showing the presence of peritectic $CaZn_{13}$ dendrites. (g) Distribution of CaZn13 fragments measured from various fields of microstructure images (the insert image 1 shows the marking of CaZn13 dendritic fragments as an example for the calculation of second phase distribution) and (h) grain size and number of grains for the binary and ternary alloys.

from the main dendrite are calculated as single entity (as shown in the inserted image of Fig. 3 - g) for the area measurement. Significantly larger dendrites occupying larger area fraction are also observed in all ternary alloys. The aim of Fig. 3 - g is to provide an approximate estimation of size of the primary phase (excluding massive dendrites) to show the effect of Cu and Ca on the growth of $CaZn_{13}$ dendrites and its distribution. As observed from the BSD images, binary Zn-0.5Ca alloy contains numerous fine fragments with a narrow size distribution and it increases simultaneously for both Ca and Cu additions in the ternary alloys. The distribution becomes much wider for Zn-1.0Ca-0.5Cu and Zn-0.5Ca-1.0Cu ternary alloys. The grain size and the grain density (number of grains/mm^2) measured for all the alloys are shown in Fig. 3 – h. Since it is evident from Fig. 2 that the grain size decreases significantly after the addition of Ca to binary and ternary alloys Fig. 2 – c, d, e, f, therefore, $CaZn_{13}$ phases could be serving as nucleation sites for the grain refinement observed. The grain size initially decreases as a function of both Ca and Cu addition, however, when the concentration of Ca or Cu is greater than 0.5 wt%, excellent refinement with equiaxed and uniform distribution of fine grains are achieved. Grain density measurement provides a better quantification of the refinement observed in the ternary alloys. It is interesting to note that within the peritectic alloys, the increase in Cu concentration from Zn-0.5Ca-0.5Cu to Zn-0.5Ca-1.0Cu provides the highest number density of grains compared to the increase occurred by the addition of Ca from Zn-0.5Ca-0.5Cu to Zn-1.0Ca-0.5Cu alloy. This indicates that the sharp rise in the number of fine grains has occurred as a function of Cu rather than Ca supplementation.

Fig. 4 – a, b shows the BSD images and compositional maps of intermetallic phases in the Ca-rich and Cu-rich ternary alloys. The mapping shows that the intermetallic phase has a rich concentration of Ca, while Cu is evenly distributed throughout the structure. The intermetallic phases are further analysed in various fields and the spectra of elements for all the ternary alloys are shown in Fig. 4 - c. These results again confirm that the intermetallic phases are rich in Ca. According to the atomic weight percent calculation, the $CaZn_{13}$ phase has 95.45 wt% Zn and 4.50 wt% Ca. The average measurement of Zn and Ca estimated through EDS point analysis (normalised wt.%) is 96.15 ± 0.6% and 3.84 ± 0.6% respectively, which correlates well with the $CaZn_{13}$ phase. Since, the Kα peak of Cu coincides with Kα of Zn, it is difficult to identify the presence of Cu within the intermetallic phase. Fig. 4 - d shows the magnified image of the EDS spectra of the Cu-containing ternary alloys (Fig. 4 - c) that indicates the presence of Cu.

Fig. 5 - a shows the XRD analysis of the binary and ternary alloys. According to the analysis performed in Fig. 4, XRD results further

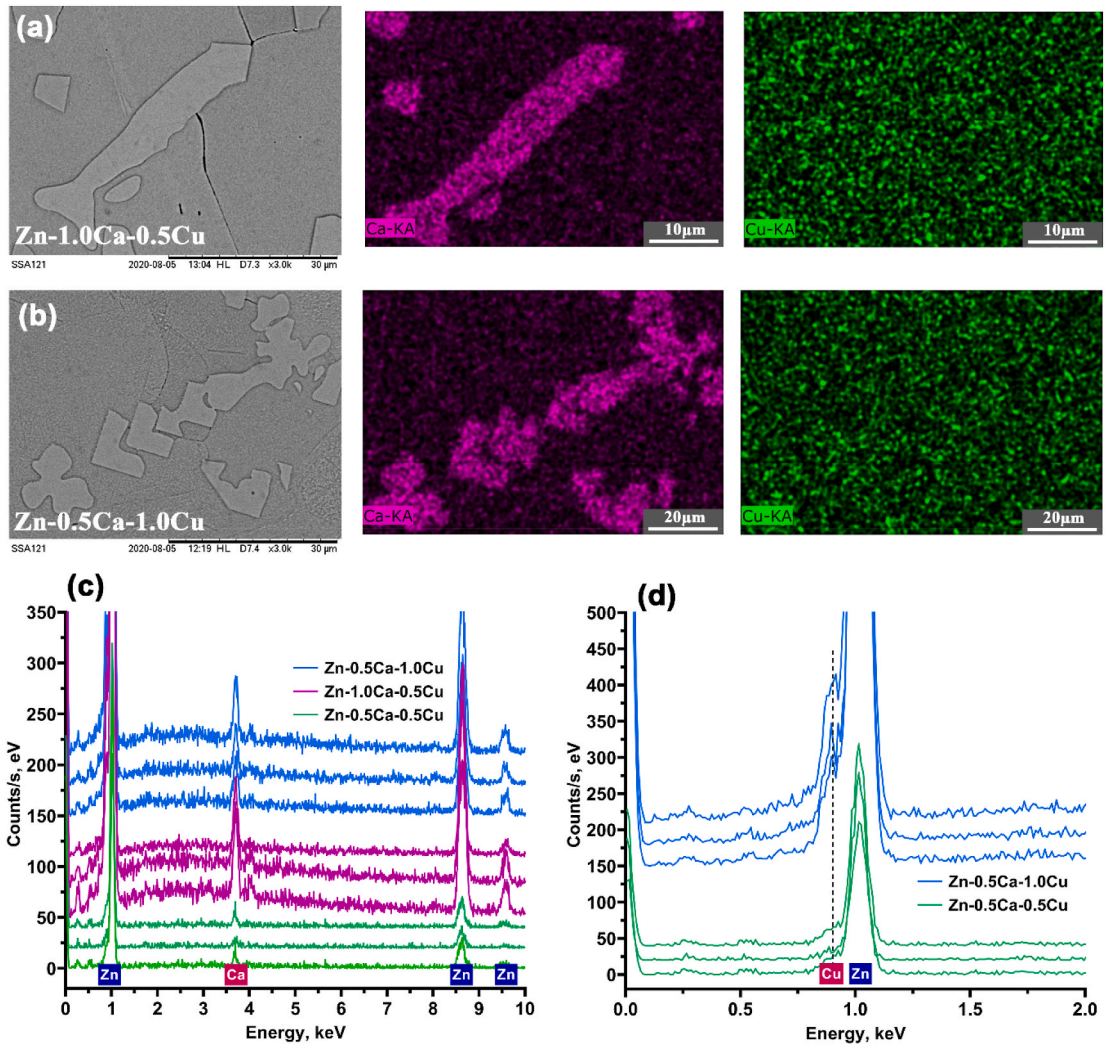

Fig. 4. Backscattered-Electron (BSE) image and elemental mapping of Ca and Cu for (a) Zn-1.0Ca-0.5Cu and (b) Zn-0.5Ca-1.0Cu alloys. (c and d) EDS spectra of point analysis examined at different locations of the sample for all the ternary alloys investigated.

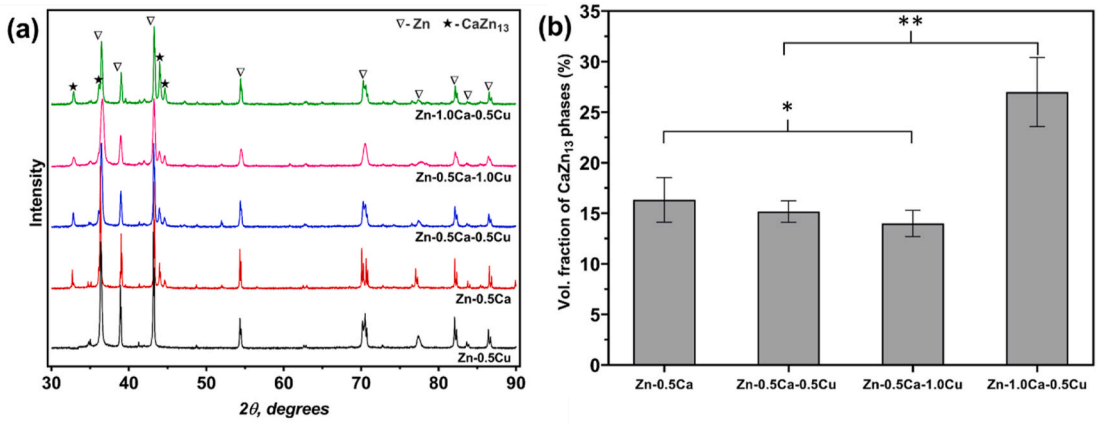

Fig. 5. (a) XRD patterns of the binary and ternary alloys used in current study; (b) volume fraction of $CaZn_{13}$ (%) in Ca-containing alloys. Asterisk represent statistical significance: **p<0.05 and*p>0.05.

confirm that the second phase in the Zn-0.5Ca alloy to be $CaZn_{13}$ with a face-centred cubic (FCC) structure. Comparing the Zn-0.5Ca to the ternary Zn–Ca–Cu alloys, the absence of additional peaks suggests that no new phases are formed after the addition of Cu to the binary Zn–Ca alloy within the levels of Cu (i.e. up to 1.0 wt%) investigated in the present work. Furthermore, the intensity of $CaZn_{13}$ peaks appears to increase with the Ca content of the ternary alloy, indicating the direct relationship of intermetallic formation with Ca concentration. Fig. 5 - b shows the relative volume fraction of the secondary phases calculated according to ASTM E562 for Ca containing binary and ternary alloys. It

is evident that the volume fraction of the second phase increases as a function of Ca addition, and the precipitate amount was nearly double in Zn-1.0Ca-0.5Cu alloy when compared to the Zn-0.5Ca-XCu (X = 0, 0.5, 1.0) alloys.

3.2. Mechanical properties

Fig. 6 shows the Vickers hardness (HV1) of the studied alloys, compared with the control, pure Zn. It can be noted that the single-phase Zn-0.5Cu alloy has the lowest hardness of 35.84HV among the alloys. This hardness value is slightly higher than that of pure Zn. The binary Zn-0.5Ca alloy displayed a significant increase in hardness compared to pure Zn and Zn-0.5Cu, due to the presence of the $CaZn_{13}$ [37]. Furthermore, the addition of the third alloying element improved the hardness of the binary alloys, with Zn-0.5Ca-1.0Cu and Zn-1.0Ca-0.5Cu exhibiting the highest hardness levels (>70HV).

Fig. 7 – a, b shows the tensile and compressive properties of pure Zn and the studied alloys, respectively. For the alloys, *YS* ranged from 10 to 20 MPa, *UTS* from 50 to 110 MPa, and elongation from 0.5 to 0.2% as shown in Fig. 7 – a. The tensile Young's modulus of Pure Zn is measured at 120 ± 3 GPa, and is increased to 132 ± 6, 152 ± 11, 132 ± 8, 156 ± 7, and 208 ± 16 GPa, for Zn-0.5Cu Zn-0.5Ca, Zn-0.5Ca-0.5Cu, Zn-0.5Ca-1.0Cu, and Zn-1.0Ca-0.5Cu alloys respectively. Furthermore, the as-cast alloys generally exhibited better compressive than tensile properties. Compared to Cu, the same amount of Ca additions offers higher strengthening effect for Zn alloys, as indicated by the relatively higher CYS of Zn-0.5Ca alloy (*CYS* = 93.4 MPa) compared to that of Zn-0.5Cu alloy (*CYS* = 42.1 MPa). The same is true when comparing the Ca rich Zn-1.0Ca-0.5Cu alloy (*CYS* = 165.61 MPa) alloy to the Cu rich Zn-1.0Cu-0.5Ca alloy (*CYS* = 144.82 MPa). *CYS* ranged from 25 to 150 MPa, *UCS* ranged from 225 to 325 Mpa (Fig. 7 – b). In general, the *YS*, *UTS* and *CYS* of the alloys appear to be proportional with alloy addition. As expected, tensile elongation (E) decreases with increasing strength. The Zn-0.5Ca and Zn-1.0Ca-0.5Cu alloys exhibited relatively lower UCS compared to pure Zn and Zn-0.5Ca-1.0Cu alloys, respectively. It is known that as cast Zn have intrinsically low tensile strength. For example, as cast pure Zn would have a typical *UTS* of about 26 MPa [46]. Indeed, such tensile weakness in cast biodegradable Zn alloys has been reported and is therefore expected [19,20].

Considering the influence of alloying elements Ca and Cu on the mechanical properties of the Zn–Ca–Cu alloys, the following observations were made. Firstly, the additions of both Ca and Cu are associated with improvements in the mechanical properties of Zn alloys. For example, the *YS*, *UTS*, *UCS* and *CYS* of the binary alloys are significantly higher than pure Zn, and the addition of third alloy element also improve the mechanical properties of the binary alloys. Secondly, compared to Cu, the addition of Ca had a more significant contribution to the improvement of *UTS* and *CYS* of the binary and ternary alloys. This is evident from the significantly higher *UTS* and *CYS* of the Zn-0.5Ca alloy (*UTS* = 60.2 MPa, *CYS* = 93.4 MPa) compared to Zn-0.5Cu alloy (*UTS* = 50.78, *CYS* = 42.1). The same is true for the ternary alloys, where the Ca-rich ternary alloy, Zn-1.0Ca-0.5Cu alloy (*UTS* = 103 MPa, *CYS* = 165.6 MPa), exhibited the highest *CYS* when compared with Zn-0.5Ca-0.5Cu alloy (*UTS* = 84.8 MPa, *CYS* = 123.6 MPa) and Zn-0.5Ca-1.0Cu alloy (*UTS* = 96.6 MPa, *CYS* = 144.8 MPa). Thirdly, the *UCS* of the alloys increases with increasing Cu content. For example, the Zn-0.5Ca-1.0Cu alloy (*UCS* = 327.3 MPa) displayed higher *UCS* than Zn-1.0Ca-0.5Cu (*UCS* = 291.7 MPa). Similar phenomenon was also observed when comparing Zn-0.5Cu and Zn-0.5Ca alloys. Finally, Cu appears to improve the structural integrity of Zn-0.5Ca alloys during compressive deformation (Supplementary information 1 (S1)). For example, with the increasing Cu content, the development of compressive rupture on Zn-0.5Ca-XCu (X = 0, 0.5, 1) occurred at higher strain during room temperature compression test. As shown in S1, the Zn-0.5Ca alloy indicated deep 'X' shaped crack at 70% compressive strain, whereas the surface of Zn-1.0Cu-0.5Ca alloy remained relatively smooth after the same condition.

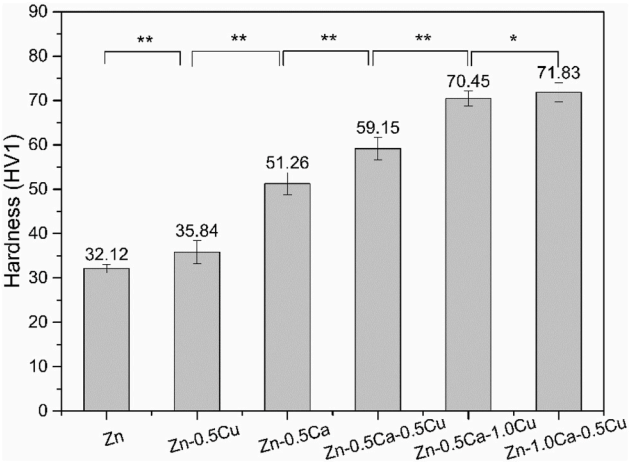

Fig. 6. The Vickers hardness (HV1) of studied alloys, asterisk represent statistical significance: **p<0.05 and*p>0.05.

3.3. Electrochemical degradation behaviour

Fig. 8 presents the open circuit potential (OCP) and potentiodynamic polarization curves of Zn, Zn-0.5Cu, Zn-0.5Ca, Zn-0.5Ca-0.5Cu, Zn-0.5-1.0Cu, and Zn-1.0Ca-0.5Cu alloys. Table 1 contains the OCP after surface stabilization was achieved, as well as the E_{corr} (V_{SCE}), icorr (μA/cm^2) and corrosion rate (μm/y) of the studied alloys that were derived from the polarization curves.

The polarization plots indicate that the E_{corr} of Zn shifted to more positive potentials after alloying with Cu and Ca. Compared to pure Zn (−1.065 V), the addition of 0.5% Cu and Ca to Zn increased the corrosion potential to −0.945 V and −0.980 V respectively, and the corrosion potential of the ternary alloys lie in between this range. Pure Zn exhibited the lowest degradation rate, *CR*, at 219 ± 5 μm/y, while Zn-0.5Cu has a slightly higher *CR* than pure Zn at 256 ± 20 μm/y. Similar to what was observed in the immersion test, the addition of Ca significantly increased the *CR* of Zn-0.5Ca alloy to 461 ± 18 μm/y, and the addition of Cu in Zn-0.5Ca alloy did not result in apparent changes in *CR*. Compared to Zn-0.5Ca-XCu (X = 0, 0.5, 1) alloys, the Zn-1.0Ca-0.5Cu possessed higher *CR* at 490 ± 15 μm/y.

Fig. 9 presents the Nyquist plots and Bode plots from the EIS measurement of the studied alloys. It can be noted that the corrosion layers formed on the alloys' surface indicated two different impendence behaviours. For pure Zn and Zn-0.5Cu alloys, two capacitive loops can be observed, where the high frequency capacitive loop indicates the charge transfer process, and the mid-frequency loop is related to the formation of a thin film on the sample's surface. Such characteristic can be fitted with the bi-layer model (Fig. 10 - a), which is a widely used equivalent circuit model describing the presence of inner and outer layer (oxidation, coating, etc.) during EIS measurement [47–50]. The bi-layer model consists of solution resistance (R_s), as well as the resistive and capacitive of the charge transfer interface (CPE_1, R_{ct}), and the outer oxidized layer (CPE_2, R_{ol}). For the Ca-containing alloys, a high frequency semi-circle capacitive loop and mid-to-low frequency depressed semicircle loop can be observed. These two characteristics are believed to result from the charge transfer process and the permeable layer, respectively. Good fits were obtained using the equivalent circuit that commonly describes effects of permeable layers on alloy surface [50–54]. As shown in Fig. 10 – b, such equivalent circuit consists of solution resistance (R_s), charge transfer process (CPE_1, R_{ct}), and the characteristics of the permeable layers (CPE_2, R_{pl}). The constant phase elements (*CPE)* are used in both models to replace the capacitors to describe the dispersive effect of the double layers [55]. The *CPE* impendence is represented by:

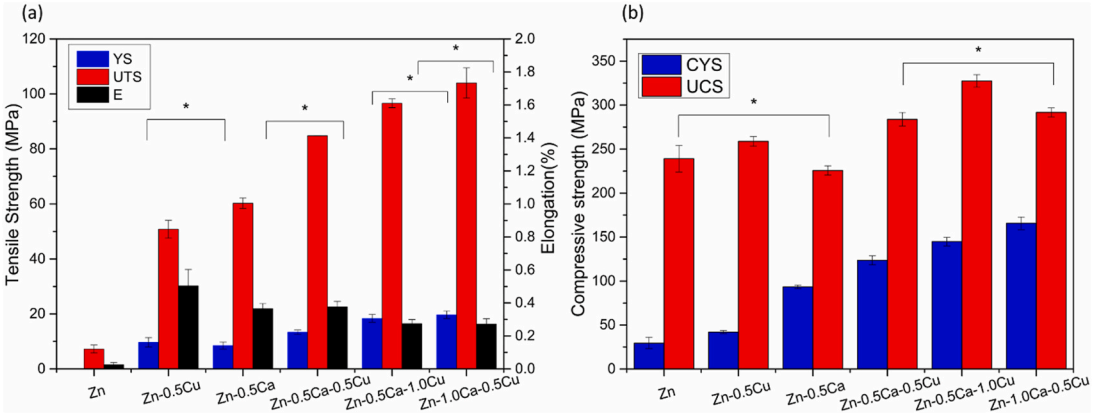

Fig. 7. The mechanical properties of studied alloys; (a): Tensile properties; *YS*-yield strength, *UTS*-ultimate tensile strength, *E*-elongation at break; (b) Compressive properties; *CYS*-compressive yield strength, *UCS*-ultimate compressive strength. The difference in data between groups are statistically significant unless otherwise indicated. *: $p > 0.05$.

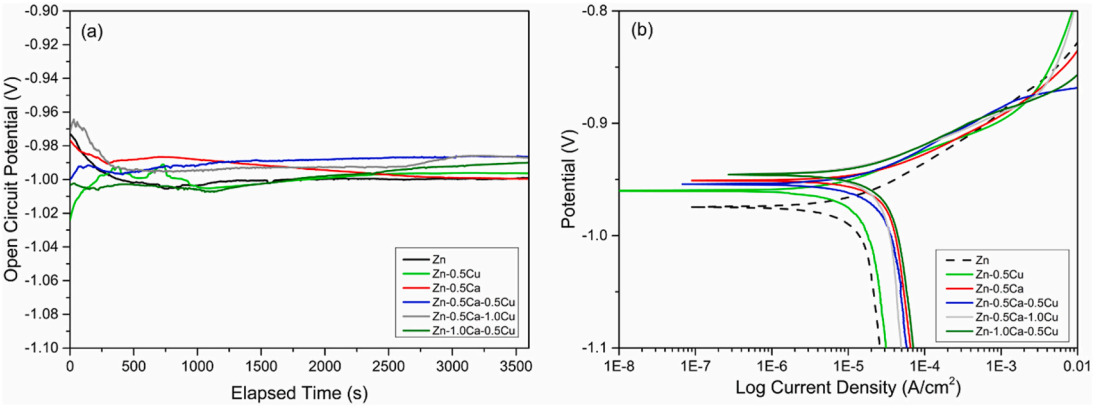

Fig. 8. The (a) Open circuit potential, and (2) electrochemical polarization curves of Zn, Zn-0.5Cu, Zn-0.5Ca, Zn-0.5Ca, Zn-0.5Ca-0.5Cu, Zn-0.5-1.0Cu, Zn-1.0Ca-0.5Cu alloys.

Table 1
Corrosion potential and corrosion rate measured from electrochemical polarization test for Zn, Zn–Ca, Zn–Cu, and Zn–Ca–Cu alloys in Hanks solution.

Material	Open circuit potential (V, vs. SCE)	Corrosion potential, E_{corr} (V, vs. SCE)	Corrosion current density i_{corr} (μA/cm^2)	Corrosion rate, *CR* (um/y)
Zn	−1.006 ± 0.010	−1.065 ± 0.007	14.598 ± 0.332	219 ± 5
Zn-0.5Cu	−0.993 ± 0.005	−0.945 ± 0.017	17.415 ± 1.361	256 ± 20
Zn-0.5Ca	−1.001 ± 0.002	−0.980 ± 0.021	30.586 ± 1.194	461 ± 18
Zn-0.5Ca-0.5Cu	−0.988 ± 0.006	−0.955 ± 0.015	30.277 ± 0.535	453 ± 8
Zn-0.5Ca-1.0Cu	−0.986 ± 0.002	−0.961 ± 0.005	31.346 ± 0.869	469 ± 13
Zn-1.0Ca-0.5Cu	−0.987 ± 0.002	−0.945 ± 0.005	32.387 ± 0.991	490 ± 15

$$Z_{CPE}=[T(j\omega)^n]^{-1} \quad (3)$$

where j is the imaginary number $(-1)^{0.5}$, ω is the angular frequency of AC signal, T is the capacitive effect of the interface, and n range between 0 and 1.

Table 2 shows the EIS circuit modelling data for pure Zn, and all studied alloys. The solution resistance (R_s) of all EIS measurements remained stable in the range of 5.22–21.45 Ω. Pure Zn showed the highest R_{ct} among all test specimens at 829.6 Ω/cm^2, and the addition of Cu increased the electrochemical activities of pure Zn, reducing its charge transfer resistance to 436.4 Ωcm^2. The R_{ct} values of the Ca-containing alloys were significantly lower compared to that of pure Zn and Zn-0.5Cu alloy. Regarding the characteristics of the corrosion layer, it can be noted that the corrosion layer on Zn–Cu alloys indicated significantly lower resistance (R_{ol}) and higher capacitance CPE_1-T compared to pure Zn. While Ca-containing alloys indicated significantly lower CPE_2-T and n values compared to that of pure Zn and Zn-0.5Cu alloy.

3.4. Immersion test

The degradation rate of Zn alloys in Hank's solution after 4 weeks and 8 weeks immersion testing is presented in Fig. 11. After 4 weeks, Zn and Zn-0.5Cu alloys show similar degradation rate at 11.5 and 12.4 μm/y respectively, which are the slowest among all test specimens. The degradation rate of Zn-0.5Ca-XCu (X = 0, 0.5, 1) alloys ranged between 18.2 and 19.8 μm/y, which were significantly higher compared to pure Zn and Zn-0.5Cu alloy. The Zn-1.0Ca-0.5Cu alloy indicated the highest degradation rate at 29.6 μm/y. After 8 weeks of immersion testing, the degradation rates of all test specimens were lower compared to the 4-weeks group, but the previously observed trends in the corrosion rate of the alloys remained the same.

Fig. 12 shows the morphology of Zn and Zn alloys after 4 and 8 weeks

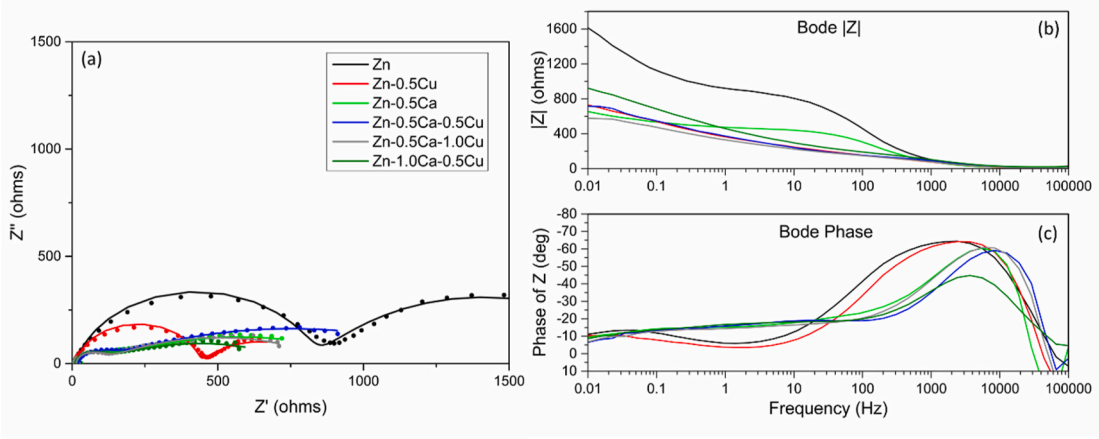

Fig. 9. The (a) Nyquist plots, (●: experiment data; —Fitted curve) and (b), (c) Bode plots of Zn, Zn-0.5Cu, Zn-0.5Ca, Zn-0.5Ca-0.5Cu, Zn-0.5-1.0Cu, and Zn-1.0Ca-0.5Cu alloys during EIS measurement.

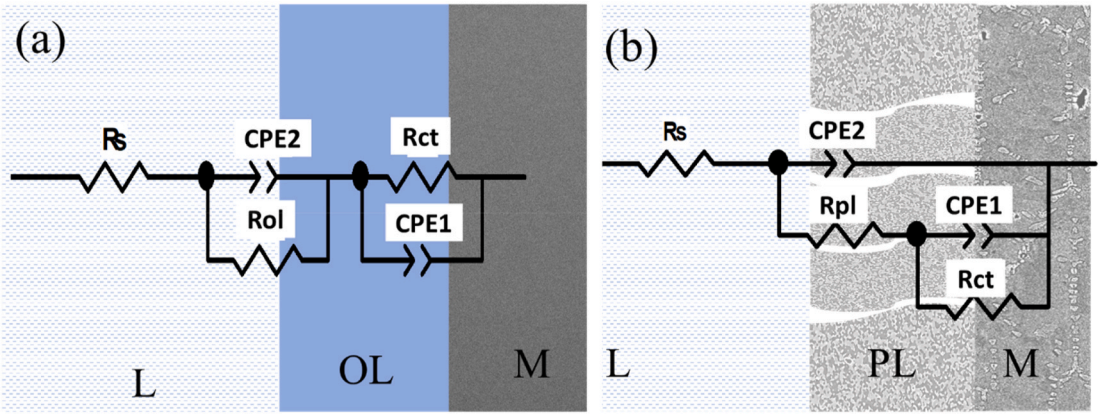

Fig. 10. Equivalent circuits used to simulate the EIS data of studied alloys: (a) Bi-layer model describing the formation of oxidation layer on Zn and Zn-0.5Ca surface; (b) Circuit describing the development of non-uniform permeable interface on Ca-containing alloys; *L*-liquid, *OL*-Oxidized layer, *PL*-permeable layer, *M*-Metal.

Table 2
Circuit parameters obtained from mathematical fitting of EIS data of the studies alloys. Values shown are the average of three measurements.

Material	R_s, Ω cm^2	CPE_1-T, μF/cm^2	n_1	R_{ct}, Ω/cm^2	$R_{ol/pl}$, Ω/cm^2	CPE_2-T, μF/cm^2	n_2	Chi square, χ^2
Zn	7.33	7.28	0.83	829.6	1270	3.07×10^3	0.59	0.0041
Zn-0.5Cu	5.22	7.51	0.85	436.4	521	1.07×10^4	0.53	0.0105
Zn-0.5Ca	8.83	1.49	0.95	60.08	802.6	1.39×10^3	0.30	0.014
Zn-0.5Ca-0.5Cu	13.23	0.99	0.91	76.92	790.2	1.26×10^3	0.37	0.027
Zn-0.5Ca-1.0Cu	9.74	1.40	0.98	68.18	734.2	1.56×10^3	0.32	0.013
Zn-1.0Ca-0.5Cu	21.45	0.92	0.96	57.69	1387	1.12×10^3	0.30	0.004

of immersion in Hank's solution. It can be noted that the metals with a single phase microstructure, such as pure Zn and Zn-0.5Cu, exhibited a relatively uniform degradation behaviour. No corrosion pits were found in the corroded surface even after prolonged immersion (8 weeks). On the other hand, the Ca-containing alloys displayed more localized degradation behaviours. For example, the Zn-0.5Ca alloy possessed deep corrosion pits on its surface after 8 weeks of immersion. For the ternary Zn-0.5Ca-0.5Cu, Zn-0.5Ca-1.0Cu, and Zn-1.0Ca-0.5Cu alloys, non-uniform degradation became evident 4 weeks after the immersion test. The second phase of these alloys were preferentially attacked during the biodegradation process, creating deep, localized corrosion pits at the interface of the second phase and the matrix. Corrosion pits were significantly larger in the Zn-1.0Ca-0.5Cu alloy compared to the other ternary alloys, which is likely associated with the high relative amounts of the second phase. After 8 weeks, the degradation of the ternary alloys continued to take place at the Zn–Cu matrix-$CaZn_{13}$ interface. The corrosion pits in the Zn-0.5Ca-XCu (X = 0.5, 1) alloys became larger and deeper, and had etched out nearly half of the second phase in these alloys. On the other hand, the Zn-1.0Ca-0.5Cu alloys experienced a more severe corrosion attack, with $CaZn_{13}$ phase completely etched out from the alloy surface, consequently resulted in faster degradation rate compared to the other ternary alloys.

Fig. 13 presents SEM images and the associated elemental maps of Zn, Ca, Cu, O, and P obtained via EDS on the cross sections of the Zn, Zn-0.5Cu, Zn-0.5Ca-0.5Cu, and Zn-1.0Ca-0.5Cu alloys after 8 weeks of immersion in Hank's solution. Fig. 13 – a, b indicates that there is a thin, dense, uniform corrosion layer formed on Pure Zn and Zn-0.5Cu alloy surface. Compared to Zn-0.5Cu alloy, the Zn-0.5Ca-0.5Cu alloy exhibited a more significant build-up of corrosion products on the surface (Fig. 13 - c). The distribution of degradation products is relatively non-

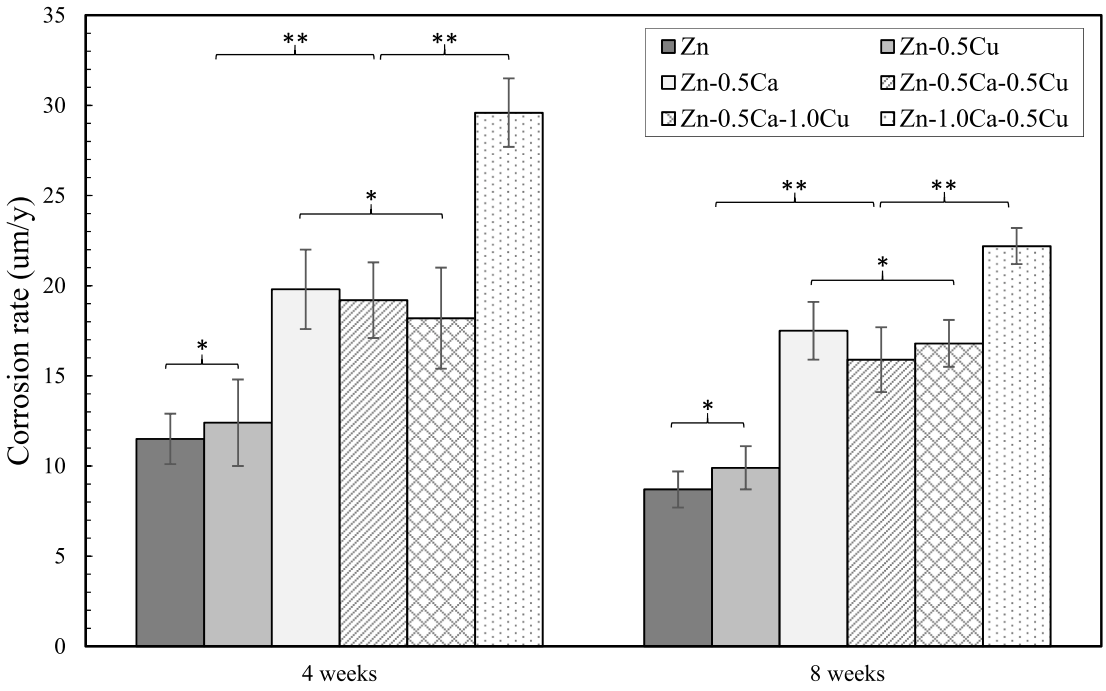

Fig. 11. The degradation rate of studied alloys after 4 and 8 weeks of immersion in Hank's solution, asterisk represent statistical significance: **p<0.05 and*>0.05.

uniform, as the thickness range between 6 and 30 μm. In addition, the presence of cracks in the corrosion layer can also be observed on Zn-0.5Ca-0.5Cu alloy. The distribution of corrosion product on Zn-1.0Ca-0.5Cu (Fig. 13 - d) appears similar to that on Zn-0.5Ca-0.5Cu alloy. However, the corrosion attack on the Zn-1.0Ca-0.5Cu alloy is more aggressive than other alloys, as some of the corrosion products extended several microns into the alloy's surface. These regions of localized accumulation of corrosion products within the alloy are believed to be the source of the corrosion pits observed in Fig. 12 - f2.

The cross-sectional element map of Zn in pure Zn, Zn-0.5Cu, Zn-0.5Ca-0.5Cu, and Zn-1.0Ca-0.5Cu (Fig. 13 - a1, b1, c1, d1) shows that there are two regions of interest: (i) the lower half region, with a rich concentration of Zn corresponding to the alloys' matrix, and the (ii) upper half section, with a low Zn concentration corresponding to the degradation products. Since the simulated physiological fluid (Hank's solution) used in this study does not contain Zn ions, therefore the Zn found in the degradation products clearly originated from the corroding metal. Similar phenomenon is also observed in Cu. Most of the Cu is found in the alloy and a small amount seen in the corrosion product (Fig. 13 - b3, c3, d3). In contrast, the distribution of Ca is non-uniform; i.e., Ca is concentrated in the corrosion product layers (Fig. 13 - a2, b2, c2, d2) as well as in some parts of the alloy's matrix (Fig. 13 - c2, d2). The high Ca concentration in the corrosion product of metals tested in physiological fluid is well known [19] and can be traced from Ca's presence in the Hank's solution. Likewise, the localized Ca concentration in the alloy matrix is due to its strong presence in the intermetallic, $CaZn_{13}$, as seen in Fig. 4. In addition, the degradation products of studied alloys also indicated high concentration of oxygen (O) (Fig. 13 - a4, b4, c4, d4), phosphorus (P) (Fig. 13 - a5, b5, c5, d5), which are also typical degradation products of metals tested in physiological environments [56]. The observed corrosion products composition through EDS analysis is consistent with published finding on the degradation products of Zn alloys, hence, the possible corrosion products on Zn are ZnO, $Zn(OH)_2$, $Zn_3(PO_4)_2$, $Ca_3(PO_4)_2$, and CaP [19,57]. In addition, the presence of Cu within the corrosion products of the Cu-containing alloys also suggest the dissolution of Cu from the alloy matrix, likely in the form of Cu_2O [58–60].

4. Discussion

4.1. Influence of Cu and Ca on the microstructure and mechanical properties

Addition of Ca and Cu to Zn produced significant grain refinement and excellent refinement with equiaxed grains obtained for all the ternary alloys. The formation of equiaxed grains are governed by two main factors (i) heterogeneous nuclei and (ii) solute [61]. Since, Ca does not have appreciable solubility and precipitates well above the equilibrium nucleation (650-600 °C) temperature of Zn-grains (420 °C), $CaZn_{13}$ intermetallic phases can act as the nucleating sites. Cu additions below the peritectic composition therefore can act as solute providing growth restriction for the grains and the nucleation of new grains by constitutional supercooling [62]. This is evident while observing the refinement produced by a Zn-0.5Ca, Zn-0.5Ca-0.5Cu and Zn-0.5Ca-1.0Cu alloys as a function of Cu additions, where Figs. 3 and 4 revealed no new intermetallic phases. On the other hand, grain refinement for the increase in Ca for a given Cu addition to Zn-0.5Cu alloy as Zn-0.5Ca-0.5Cu and Zn-1.0Ca-0.5Cu becomes saturated. Therefore, it is evident that Ca and Cu collectively contributed to the refinement of Zn–Ca–Cu ternary alloys reducing the grain size to less than 150 μm. The synergistic effect of $CaZn_{13}$ as nucleant and Cu as solute were identified as the contributing factors for the significant refinement of Zn–Ca–Cu alloys.

The strengthening of Zn-0.5Ca and Zn-0.5Cu binary alloys can be attributed to (1) second phase strengthening that result from the formation of $CaZn_{13}$ within the matrix, and (2) solid solution strengthening, as the 0.5 wt% content is still below Cu's maximum solubility in Zn. Compared to the binary alloys, the ternary alloys in the present study indicated much higher *CYS* and *YS*. In addition to the combined effect of the previously mentioned strengthening mechanisms, the refined grain size in the ternary alloys further improved the strength of the ternary alloys through grain boundary strengthening, as described by Hall-Petch relationship [63]. The increase hardness values are evident with the addition of Ca and Cu into the ternary Zn–Ca–Cu alloys. It was reported that the microhardness of $CaZn_{13}$ is 223 HV1, which is nearly four times higher than that of pure Zn [64]. Therefore, the increase in hardness

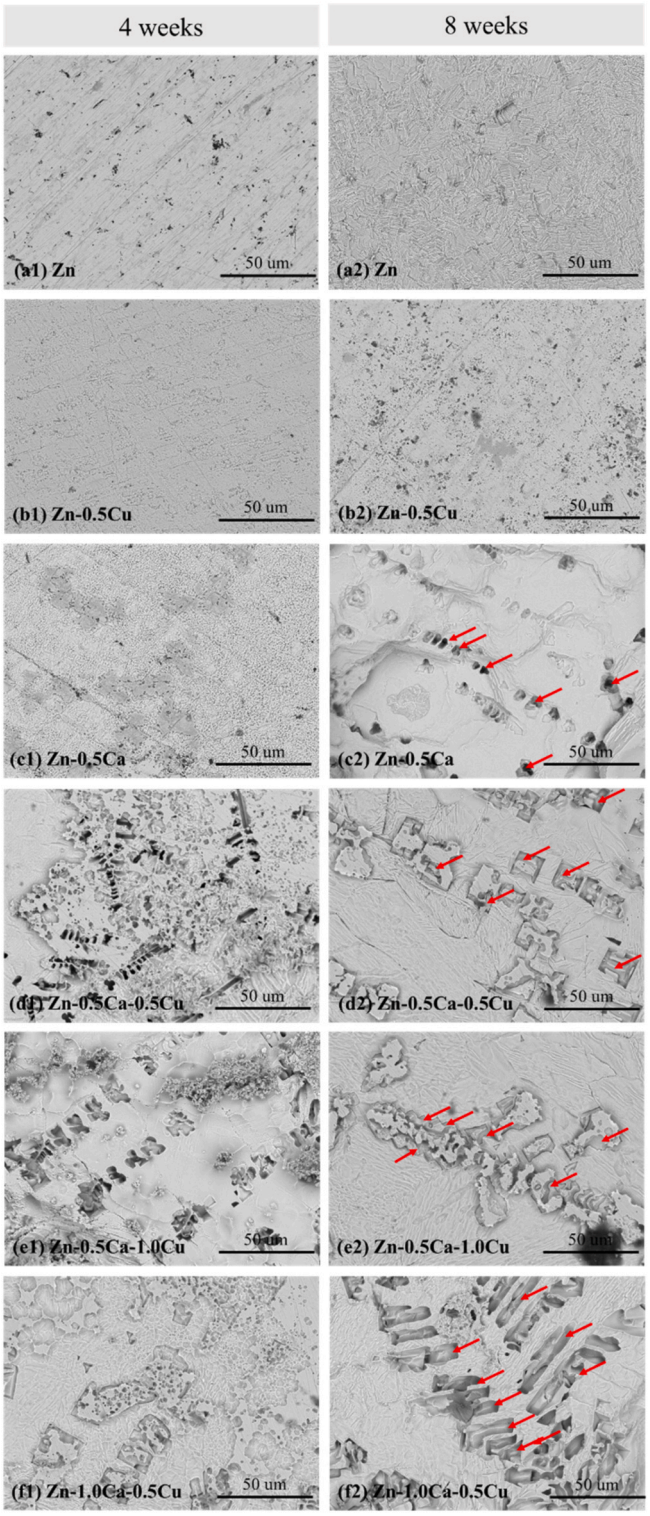

Fig. 12. The corrosion morphology of (a) Zn, (b) Zn-0.5Cu, (c) Zn-0.5Ca, (d) Zn-0.5Ca-0.5Cu, (e) Zn-0.5-1.0Cu, (f) Zn-1.0Ca-0.5Cu after 4 (Left) and 8 (Right) weeks of immersion in Hank's solution. Red arrows indicate the corrosion pits.

from Ca addition can be easily attributed to the increase in the fraction of second phase $CaZn_{13}$. The effect of Cu addition below 2% on the hardness of Zn alloys has not been reported previously. According to the current study, it can be noted that 0.5–1 wt% Cu also improved the hardness of Zn-0.5Ca alloy, likely by increasing the hardness of the Zn–Cu matrix which is evident in the binary Zn-0.5Cu alloy.

After the addition of 0.5 Cu to pure Zn, there is no significant change observed in the refinement of grain structure. Columnar grains were predominant in the microstructure and the Zn-0.5Cu alloy still exhibited single-phase microstructure, albeit a notable increase in the *YS*, *UTS*, *UCS* and elongation have occurred. Therefore, the increase in properties can be attributed to the solid solution strengthening of Cu in Zn [35]. On the other hand, the strengthening effect from Ca addition is attributed to the formation of $CaZn_{13}$ phase, as several studies have reported that the precipitated $CaZn_{13}$ phase can significantly improve the strength of Zn alloys by increasing dislocation density and hindering dislocations motions within the alloys [65–67]. Although the average grain size is reduced, the microstructure of Zn-0.5 Ca alloys exhibits a mixed structure of fine columnar grains and small number of equiaxed grains. It is well-known that reducing the secondary dendritic arm spacing and grain size contributes to the increase in mechanical strength of the alloys [68]. In addition, it should be noted that a decrease in grain size could not solely account for the improved mechanical properties in the microstructures where precipitates are present. The size distribution and the amount of phase also contributes to the strength of the as-cast alloys [69]. A Zn–3Cu-(0.5, 1.0)Fe alloys containing peritectic dendrites of FeZn13 and CuZn5 phases [70] and a Zn-0.75Mn-0.4Cu alloy containing Zn–Mn–Cu phases [71] are typical examples in Zn alloys where pro-peritectic phases grow as dendrites or needle shaped phases that cause a significant drop in the mechanical properties. This is also true for all the ternary alloys investigated in the present work where the grain size is decreased while the precipitation of $CaZn_{13}$ dendrites becomes larger in size and increased in the area fraction (SEM images in Fig. 3 – c-f). $CaZn_{13}$ dendrites assumes the FCC crystal structure and can easily grow into large dendritic phases in Zn [72], it is therefore considered to be the cause of early fracture/rupture in Zn–Ca alloys during deformation [36]. In the present study, the lower values of *UCS* of Ca rich Zn-1.0Ca-0.5Cu and Zn-0.5Ca alloy and tensile elongation in ternary alloys are likely due to the presence of coarse $CaZn_{13}$ phases that acted as crack nucleation points.

Table 3 presents the mechanical properties of the studied alloys in comparison to pure Zn, Zn-nutrient elements alloy systems, and some absorbable/non-absorbable metallic wound closure devices. Both Zn and Mg-based materials have been investigated as the absorbable alternative to traditional Ti-based staples for gastric anastomosis applications. For example, the fabrication of absorbable surgical staples from high purity Mg and Mg-Nd-Y alloy were reported by Wu et al. [76], Qu et al. [75]. and Amano et al. [77]. These materials possess UTS of 196–290 MPa, elongation of 14.6–22.0%, which exhibited sufficient tensile force and biocompatibility in the animal gastrointestinal environment. Similarly, Zn based staples (Zn–Cu–Mn–Ti, Zn–Mn–Ti, Zn–Cu–Ti) with UTS of 198–212 MPa and elongation of 7–21% were also found to provide a good combination of strength, biodegradability and biocompatibility to stomach closure in an animal study [78]. Judging by the mechanical properties of pure Zn and Zn alloys in Table 3, it is clear that the strength of the as cast Zn alloys can hardly satisfy the mechanical property requirements for wound closure application. Nevertheless, the strength of Zn alloys can be markedly increased after traditional or advanced wrought processing. For example, the *UTS* of as cast Zn–3Mg and Zn-1.0Mg-0.1Mn - which exhibited similar values to the Zn–Ca–Cu alloys in the current study - experienced a more than 2.5-fold increase after thermal wrought processing [74,81]. The *YS* and *E* of Zn–Ca–Cu alloys are also expected to be improved after casting defects and microstructural non-uniformities are eliminated through deformation processing. On the other hand, the investigation on biodegradable metallic sutures is still at the preliminary stage, and the mechanical properties of the fabricated Zn [18] and Mg [79] based wires are still well below that of 316 stainless steel sutures [80]. Hence, the applicability of the studied Zn–Ca–Cu alloys for suture application may still be limited. The refinement and the distribution of fine peritectic dendrites through deformation processing is further suggested to develop better yield strength and ductility in these ternary alloys.

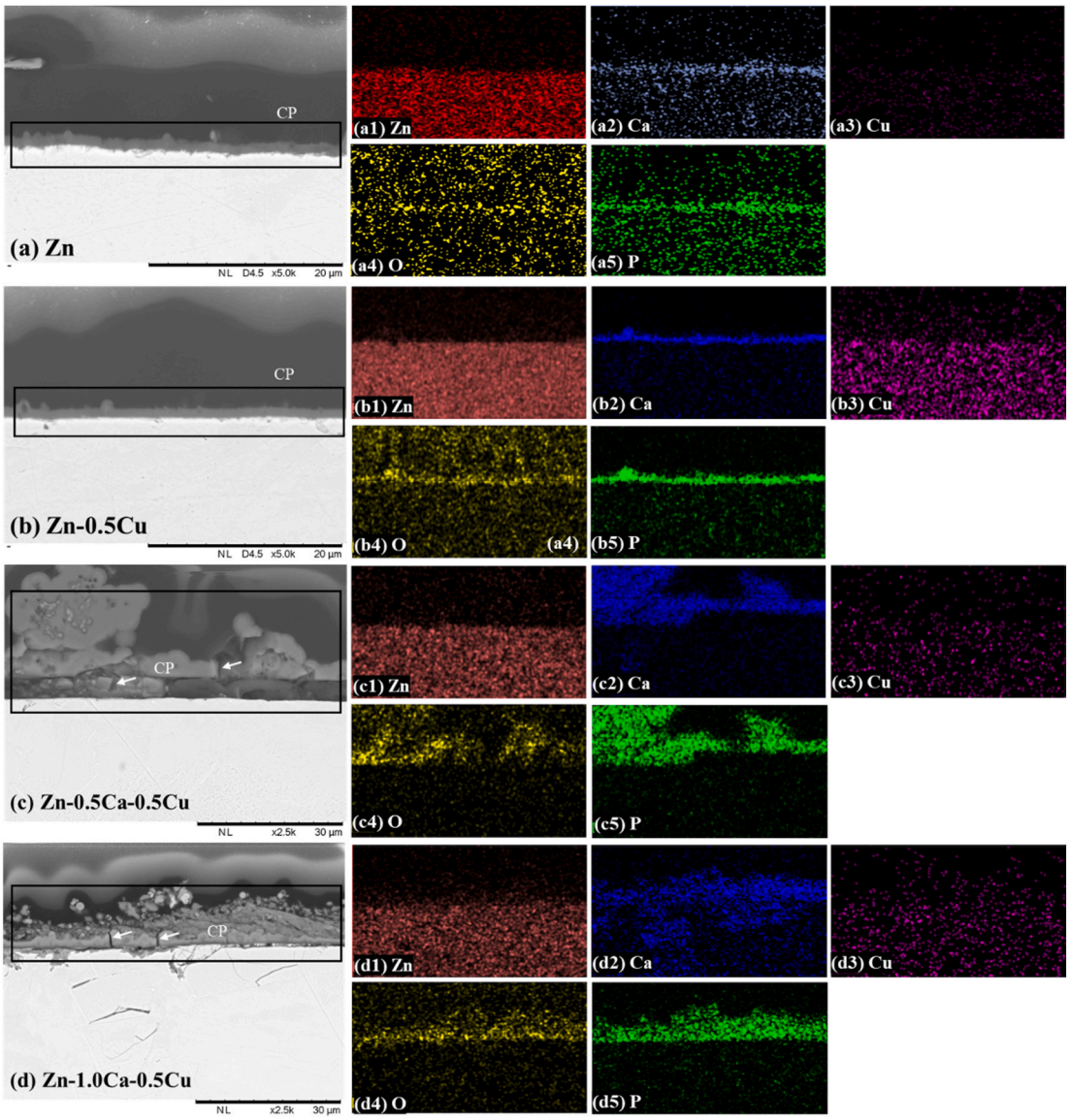

Fig. 13. BSD image and elemental mapping of Zn, Ca, Cu, O and P for the cross section of (a) Zn, (b) Zn-0.5Cu, (c) Zn-0.5Ca-0.5Cu, and (d) Zn-1.0Ca-0.5Cu alloys after 8 weeks of immersion in Hank's solution. *CP*, corrosion products; White arrow mark: cracks within the corrosion product.

4.2. Degradation behaviour

In the current study, the degradation of the Zn–Ca–Cu alloy in a simulated physiological fluid (Hank's solution) was confirmed. It was observed that, compared to Ca, the influence of Cu addition on the degradation properties of Zn is minor. No significant difference can be seen in the corrosion rate and the corrosion morphology between pure Zn and Zn-0.5Cu. The observed composition of degradation products (P, O, Ca, Cu, Zn) from Zn–Cu alloy is consistent with the published *in vitro* corrosion behaviour of similar alloy systems [57,70,71]. Compared to pure Zn, the corrosion product layer on Zn–Cu alloy indicated significantly decreased resistance and increased capacitance. These changes are likely associated with the presence Cu within the corrosion products of Zn-0.5Cu alloy. Nevertheless, the formation of a compact, uniform corrosion product layer on the alloy surface provided some protection to the Zn-0.5Cu matrix - similar to what was observed on pure Zn - and resulted in the observed low corrosion rate.

Ca, on the other hand, has a confirmed role in increasing the corrosion rate of Zn alloys by promoting intermetallic phase galvanic corrosion ($Zn/CaZn_{13}$) [21,37]. Compared to the single phase pure Zn and Zn-0.5Cu alloy, the intermetallic galvanic corrosion increased the speed of the charge transfer process occurred on alloy's surface, and resulted in the observed low R_{ct} values of the Ca-containing alloys. Such observation suggest that the Ca-bearing alloys intrinsically possess lower corrosion resistance [82], hence, indicated faster corrosion rate. Assuming that the corrosion rate is mainly influenced by the addition of Ca, Fig. 14 shows the corrosion trend plotted for the intermetallic phase fraction area against the immersion test results. With the increase in the fraction of intermetallic phases, the rate of corrosion increases linearly for 4 and 8 weeks experiments. The slope of linear fit for 4 week is higher (0.65 μm/y·(%)) compared to the 8 week sample (0.50 μm/y·(%)) indicating the formation of the more passivated layer, however, the trend remains linear. Zou et al. also noted that the corrosion rate of Zn–Ca alloys increases with increasing Ca concentration, i.e. by increasing the volume fraction of $CaZn_{13}$ dendrites [37].

The presence of Ca in Zn alloys altered the characteristics of the corrosion products, as evident from Fig. 13, where the corrosion products on Ca-containing alloys are significantly thicker, less uniform, and with more cracks compared to those layers found in the Zn and Zn-0.5Cu alloys. Similar phenomena were also expected to occur in the Ca-

Table 3
Mechanical properties of studied alloys, reported pure Zn and Zn-nutrient element alloys, and absorbable/nonabsorbable metallic wound closure devices.

Material	YS (MPa)	UTS (MPa)	E (%)	Source
Pure Zn^{C}	–	29.4	0.2	[46]
Pure Zn^{E}	129.6	180.0	54.0	
Zn-3.0 Mg^{C}	65	84	1.3	[73]
Zn-3.0 Mg ^{ECAP}	205	220	6.3	
Zn-1.0Mg-0.1Mn^{C}	114.10	131.94	1.11	[74]
Zn-1.0Mg-0.1Mn^{R}	195.02	299.04	26.07	
Zn-0.5Ca-0.5Cu^{C}	13.3	84.8	0.37	Present
Zn-0.5Cu-1.0Cu^{C}	18.4	96.6	0.28	paper
Zn-1.0Ca-0.5Cu^{C}	19.7	104.0	0.27	
Biodegradable metallic staple (Mg-based)	147–260	196–290	14.6–22.0	[75–77]
Biodegradable metallic staple (Zn-based)	177–196	198–212	7–21	[78]
Mg-based sutures^{E,D} (ø 0.27 mm)		206–458	9.4–14.4	[79]
Pure Zn suture^{E,D} (ø0.3 mm)	73.62	100.09	15.95	[18]
316 Stainless steel sutures	170–310	480–620	30–40	[80]

C: as cast; E: extruded; ECAP- equal channel angular pressing, R: hot rolled, D: drawned.

containing alloys at the initial stage of biodegradation, judging by the *CPE* behaviours of the corrosion layer. The CPE_2 values of the corrosion layer, as shown in Table 2, indicate that the Ca-containing alloys exhibited lower CPE_2-*T* and *n* values compared to pure Zn and Zn–Cu alloy. Although the origin of the *CPE* behaviour in EIS measurement is still under debate, it is generally attributed to the time-constant distributions caused by interfacial heterogeneity, e.g. surface roughness [83], electrode porosity [84], the extent of which is determined by deviation of the CPE exponent *n* from the ideal capacitive behaviour $n = 1$. Hence, the small CPE exponent *n* obtained for the corrosion layers developed on Ca-containing alloys surfaces is possibly related to the higher level of surface inhomogeneity/porosity. CPE_2-*T* represents the capacitive effect of the corrosion layer and is inversely proportional to the thickness of the corrosion products, assuming the corrosion products on all Ca-containing alloys possess similar electrical permittivity [85]. Therefore, the lower CPE_2-*T* values obtained from EIS analysis for Ca-containing alloys may provide another indication of the formation of thicker corrosion products due to Ca addition.

Fig. 15 presents a schematic of the proposed evolution of the biodegradation process of Zn-0.5Cu and Zn-0.5Ca-0.5Cu alloy in comparison to pure Zn in Hank's solution. As shown in Fig. 15 – a1, the degradation Zn in simulated body fluid is well known to proceed following anodic reaction [10]:

$$Zn \rightarrow Zn^{2+} + 2e^{-} \quad (4)$$

And cathodic reaction:

$$O_2 + 2H_2O + 4e^{-} \rightarrow 4OH^{-} \quad (5)$$

And the corrosion products formation in Fig. 15 – a2 mainly involves:

$$Zn^{2+} + 2OH^{-} \rightarrow Zn(OH)_2 \quad (6)$$

And

$$Zn(OH)_2 \rightarrow ZnO + H_2O \quad (7)$$

Meanwhile, ZnO and $Zn(OH)_2$ can redissolve into Zn^{2+} due to the presence of chloride, and further interact with the Ca^{2+}, $H_2PO_4^{-}$, HPO_4^{2-}, HCO_3^{2-} in Hank's solution [19,56], and eventually result in the formation of Ca, O, P, C-rich complex compounds as observed in Fig. 13.

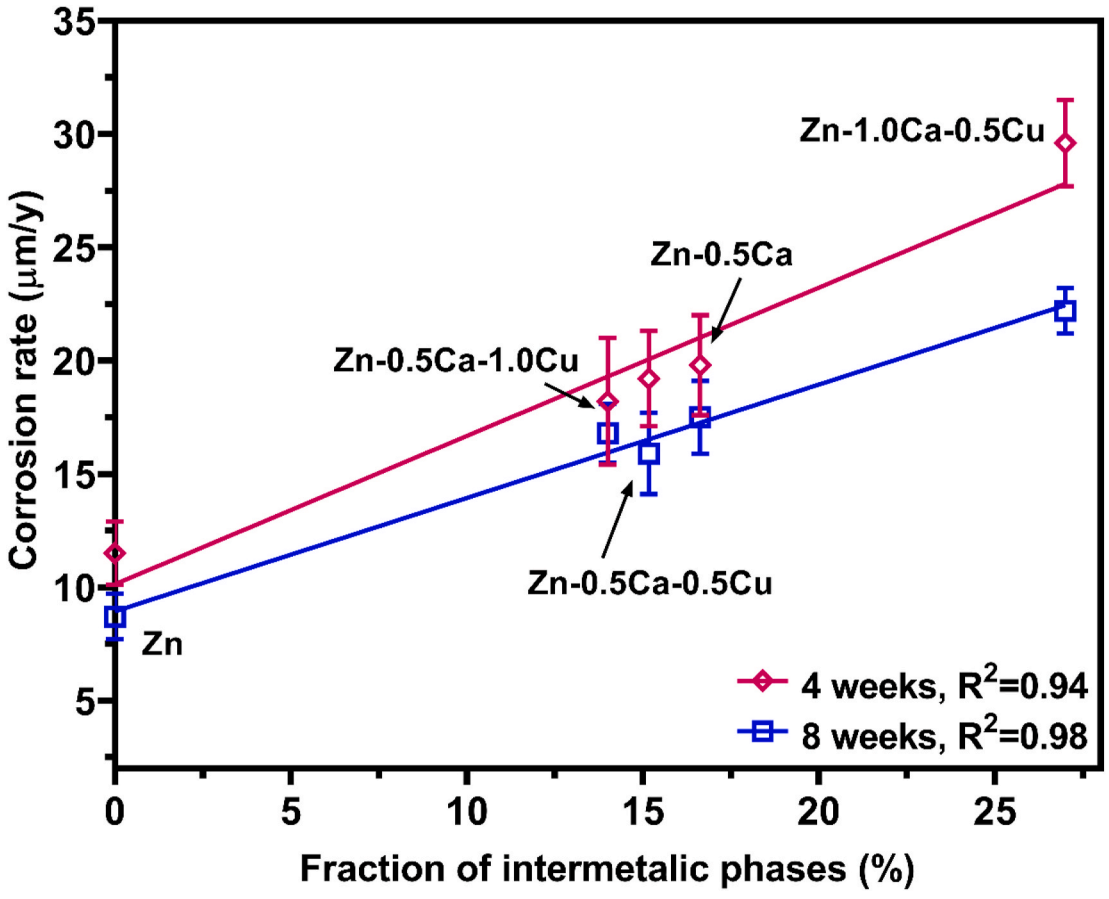

Fig. 14. Corrosion rate as a function of area fraction of intermetallic phases calculated in Fig. 5 – b.

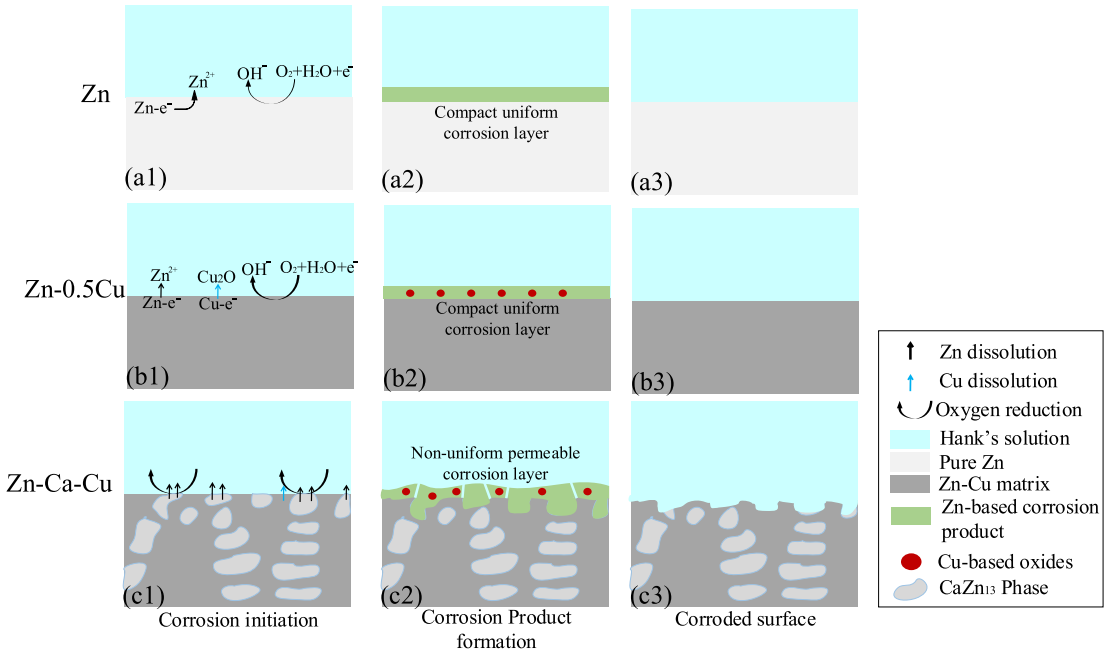

Fig. 15. Schematic diagram of the evaluation of biodegradation process of (a) Zn, (b) Zn-0.5Cu, and (c) studied ternary Zn–Ca–Cu alloys in Hank's solution.

The presence of additional Cu within the corrosion products of Zn-0.5Cu alloy compared to pure Zn suggest that, in addition to the reaction (3), (4), (5), (6), Cu may have also participated in the biodegradation process as solute atoms within Zn matrix, as shown in Fig. 15 – b1, b2. The corrosion of pure Cu in simulated physiological fluid were investigated in several studies [58,60], which is found to proceed via the following reactions:

$$\text{Oxide formation: } 8Cu + 2H_2O + O_2 \rightarrow 4Cu_2O + 4H^+ + 4e^- \quad (8)$$

And

$$\text{oxide dissolution: } Cu_2O + 2H_2O \rightarrow 2Cu^{2+} + H_2O + 2e^- \quad (9)$$

These reactions provide possible explanations for the presence of Cu within the corrosion products of Zn-0.5Cu alloy. However, regardless of the slight difference in corrosion mechanism between pure Zn and Zn-0.5Cu alloy, uniform corrosion is expected on both materials due to the homogeneity of microstructures, which corresponds to the observed uniform corrosion morphology as presented in Fig. 13 – a, b and Fig. 15 – a3, b3.

In contrast, the corrosion of ternary Zn–Ca–Cu alloys proceeds in a less uniform manner due to the micro-galvanic corrosion between the Zn–Cu matrix and $CaZn_{13}$ phase. As shown in Fig. 15 – c1, the $CaZn_{13}$ phase was preferably attacked during immersion in Hanks's solution, which led to the formation of bulky corrosion products on top and within the intermetallic phase. On the other hand, the corrosion attack on the Zn–Cu matrix was less aggressive than that on the intermetallic phase. Therefore, the build-up of corrosion products occurred at different rates on different phases, which then led to the formation of a non-uniform, permeable corrosion layer with the presence of cracks, as shown in Fig. 15 – c2 and Fig. 13 – c, d. In summary, the increased corrosion rates in the Ca-bearing alloys can be attributed to: (1) the increased micro-galvanic corrosion activities through the formation of $CaZn_{13}$, and (2) the formation of a less protective, permeable corrosion layer on the alloy's surface. Nevertheless, the increased corrosion rate of the ternary alloys from Ca addition is considered to be an advantage to accelerate the degradation rate of biodegradable metallic staples to enable suitable strength retention period that coincides with that of soft tissue healing time and reduce unnecessary implant retention within the tissue [16].

In this study, the degradation rate of test specimens measured by the immersion test and electrochemical test had significant differences in terms of quantitative value. It should be noted that the mechanisms by which the corrosion rate is assessed by these two techniques are fundamentally different. The corrosion rate calculated by weight loss after immersion test is an average value over the exposure period (assuming uniform corrosion occurred on surface), while the electrochemical polarization tests are conducted for a short period with potential applied on the test specimen. Nevertheless, immersion testing and electrochemical measurement indicated a similar trend in terms of the influence of Ca and Cu on the degradation rate of Zn alloys.

5. Conclusion

In this study, Zn–Ca–Cu alloys that are targeted for wound closure device applications were fabricated and characterized. Microstructure analysis revealed that the ternary alloys (i.e. Zn-0.5Ca-0.5Cu, Zn-1.0Ca-0.5Cu, Zn-1.0Cu-0.5Ca) consist of $CaZn_{13}$ dendrites distributed within the Zn–Cu solid solution. The area fraction and relative volume of $CaZn_{13}$ increased with increasing Ca content, which induced extensive micro-galvanic corrosion in the host phase during biodegradation process, and is considered as the major factor that influence the degradation characteristics of the ternary alloys.

Compared to Zn–Ca and Zn–Cu binary alloys, the ternary Zn–Ca–Cu alloys demonstrated improved mechanical properties due to the combined effects of solid solution strengthening, grain size strengthening, and second phase hardening. The Zn-1.0Ca-0.5Cu alloy in particular, exhibited promising characteristics for the fabrication of wound closure device, which are indicated by its refined grain size and crack-free structure after significant compressive deformation at room temperature, in addition, the increased corrosion rate of the ternary alloys from Ca addition is considered to be an advantage for biodegradable staple application.

The as cast Zn–Ca–Cu ternary alloys are still facing several challenges before its adoption for practical wound closure device applications. Future research is geared on investigating processing techniques that will induce favourable microstructures (e.g. refined intermetallic dendrite structure, refined grain structure, pore and void-free lattice) and enhance the ensuing mechanical and corrosion properties of the

Zn–Ca–Cu alloys.

CRediT authorship contribution statement

Nan Yang: Conceptualization, Validation, Formal analysis, Investigation, Writing - original draft. **Nagasivamuni Balasubramani:** Formal analysis, Investigation, Writing - original draft. **Jeffrey Venezuela:** Conceptualization, Writing - review & editing, Supervision. **Sharifah Almathami:** Writing - review & editing. **Cuie Wen:** Writing - review & editing. **Matthew Dargusch:** Resources, Writing - review & editing, Funding acquisition, Supervision.

Declaration of competing interest

The authors declare that they have no known competing financial interests or personal relationships that could have influenced the work reported in this paper.

Acknowledgement

N. Yang, N Balasubramani, J. Venezuela, S Almathami, and M. Dargusch acknowledge the support of the Australian Research Council through the ARC Research Hub for Advanced Manufacturing of Medical Devices (IH150100024).

Appendix A. Supplementary data

Supplementary data to this article can be found online at https://doi.org/10.1016/j.bioactmat.2020.10.015.

References

[1] A.L. Tajirian, D.J. Goldberg, A review of sutures and other skin closure materials, J. Cosmet. Laser Ther. 12 (6) (2010) 296–302, https://doi.org/10.3109/14764172.2010.538413.
[2] L. Al-Mubarak, M. Al-Haddab, Cutaneous wound closure materials: an overview and update, J. Cutan. Aesthetic Surg. 6 (4) (2013) 178–188, https://doi.org/10.4103/0974-2077.123395.
[3] Y. Li, J. Yan, W. Zhou, P. Xiong, P. Wang, W. Yuan, Y. Zheng, Y. Cheng, In vitro degradation and biocompatibility evaluation of typical biodegradable metals (Mg/Zn/Fe) for the application of tracheobronchial stenosis, Bioactive Mater. 4 (2019) 114–119, https://doi.org/10.1016/j.bioactmat.2019.01.001.
[4] H. Kabir, K. Munir, C. Wen, Y. Li, Recent research and progress of biodegradable zinc alloys and composites for biomedical applications: biomechanical and biocorrosion perspectives, Bioactive Mater. 6 (3) (2021) 836–879, https://doi.org/10.1016/j.bioactmat.2020.09.013.
[5] Y. Sun, H. Wu, W. Wang, R. Zan, H. Peng, S. Zhang, X. Zhang, Translational status of biomedical Mg devices in China, Bioactive Mater. 4 (2019) 358–365, https://doi.org/10.1016/j.bioactmat.2019.11.001.
[6] C. Gao, M. Yao, C. Shuai, S. Peng, Y. Deng, Nano-SiC reinforced Zn biocomposites prepared via laser melting: microstructure, mechanical properties and biodegradability, J. Mater. Sci. Technol. 35 (11) (2019) 2608–2617, https://doi.org/10.1016/j.jmst.2019.06.010.
[7] B. Jia, H. Yang, Y. Han, Z. Zhang, X. Qu, Y. Zhuang, Q. Wu, Y. Zheng, K. Dai, In vitro and in vivo studies of Zn-Mn biodegradable metals designed for orthopedic applications, Acta Biomater. 108 (2020) 358–372, https://doi.org/10.1016/j.actbio.2020.03.009.
[8] C. Shuai, S. Li, S. Peng, P. Feng, Y. Lai, C. Gao, Biodegradable metallic bone implants, Mater. Chem. Front. 3 (4) (2019) 544–562, https://doi.org/10.1039/C8QM00507A.
[9] J.M. Seitz, M. Durisin, J. Goldman, J.W. Drelich, Recent advances in biodegradable metals for medical sutures: a critical review, Adv. Healthc. Mater. 4 (13) (2015) 1915–1936, https://doi.org/10.1002/adhm.201500189.
[10] Y.F. Zheng, X.N. Gu, F. Witte, Biodegradable metals, Mater. Sci. Eng. R Rep. 77 (2014) 1–34, https://doi.org/10.1016/j.mser.2014.01.001.
[11] D. Persaud-Sharma, A. McGoron, Biodegradable magnesium alloys: a review of material development and applications, J. Biomim. Biomater. Tissue Eng. 12 (2012) 25–39. https://doi.org/10.4028/www.scientific.net/JBBTE.12.25.
[12] F. Witte, The history of biodegradable magnesium implants: a review, Acta Biomater. 6 (5) (2010) 1680–1692, https://doi.org/10.1016/j.actbio.2010.02.028.
[13] A. Francis, Y. Yang, S. Virtanen, A.R. Boccaccini, Iron and iron-based alloys for temporary cardiovascular applications, J. Mater. Sci. Mater. Med. 26 (3) (2015) 138, https://doi.org/10.1007/s10856-015-5473-8.
[14] Y.K. Kim, K.B. Lee, S.Y. Kim, K. Bode, Y.S. Jang, T.Y. Kwon, M.H. Jeon, M.H. Lee, Gas formation and biological effects of biodegradable magnesium in a preclinical and clinical observation, Sci. Technol. Adv. Mater. 19 (1) (2018) 324–335, https://doi.org/10.1080/14686996.2018.1451717.
[15] M. Peuster, C. Hesse, T. Schloo, C. Fink, P. Beerbaum, C. von Schnakenburg, Long-term biocompatibility of a corrodible peripheral iron stent in the porcine descending aorta, Biomaterials 27 (28) (2006) 4955–4962, https://doi.org/10.1016/j.biomaterials.2006.05.029.
[16] J.J.D. Venezuela, S. Johnston, M.S. Dargusch, The Prospects for Biodegradable Zinc in Wound Closure Applications, Advanced Healthcare Materials, 2019, e1900408, https://doi.org/10.1002/adhm.201900408.
[17] H.F. Li, X.H. Xie, Y.F. Zheng, Y. Cong, F.Y. Zhou, K.J. Qiu, X. Wang, S.H. Chen, L. Huang, L. Tian, L. Qin, Development of biodegradable Zn-1X binary alloys with nutrient alloying elements Mg, Ca and Sr, Sci. Rep. 5 (2015) 10719, https://doi.org/10.1038/srep10719.
[18] H. Guo, R.H. Cao, Y.F. Zheng, J. Bai, F. Xue, C.L. Chu, Diameter-dependent in vitro performance of biodegradable pure zinc wires for suture application, J. Mater. Sci. Technol. 35 (8) (2019) 1662–1670, https://doi.org/10.1016/j.jmst.2019.03.006.
[19] J. Venezuela, M.S. Dargusch, The influence of alloying and fabrication techniques on the mechanical properties, biodegradability and biocompatibility of zinc: a comprehensive review, Acta Biomater. 87 (2019) 1–40, https://doi.org/10.1016/j.actbio.2019.01.035.
[20] G. Li, H. Yang, Y. Zheng, X. Chen, J. Yang, D. Zhu, L. Ruan, K. Takashima, Challenges in the use of zinc and its alloys as biodegradable metals: perspective from biomechanical compatibility, Acta Biomater. (2019), https://doi.org/10.1016/j.actbio.2019.07.038.
[21] H. Yang, B. Jia, Z. Zhang, X. Qu, G. Li, W. Lin, D. Zhu, K. Dai, Y. Zheng, Alloying design of biodegradable zinc as promising bone implants for load-bearing applications, Nat. Commun. 11 (1) (2020) 401, https://doi.org/10.1038/s41467-019-14153-7.
[22] Y. Liu, Y. Zheng, X. Chen, J. Yang, H. Pan, D. Chen, L. Wang, J. Zhang, D. Zhu, S. Wu, K.W.K. Yeung, R. Zeng, Y. Han, S. Guan, Fundamental theory of biodegradable metals—definition, criteria, and design, Adv. Funct. Mater. 29 (18) (2019) 1805402, https://doi.org/10.1002/adfm.201805402.
[23] C. Dennis, S. Sethu, S. Nayak, L. Mohan, Y. Morsi, G. Manivasagam, Suture materials — current and emerging trends, J. Biomed. Mater. Res. 104 (6) (2016) 1544–1559, https://doi.org/10.1002/jbm.a.35683.
[24] K. Kaur, R. Gupta, S.A. Saraf, S.K. Saraf, Zinc: the metal of life, Compr. Rev. Food Sci. Food Saf. 13 (4) (2014) 358–376, https://doi.org/10.1111/1541-4337.12067.
[25] P.h. Lin, M. Sermersheim, H. Li, P. Lee, S.M. Steinberg, J. Ma, Zinc in wound healing modulation, Nutrients 10 (1) (2017) 16, https://doi.org/10.3390/nu10010016.
[26] A.B.G. Lansdown, U. Mirastschijski, N. Stubbs, E. Scanlon, M.S. Ågren, Zinc in wound healing: theoretical, experimental, and clinical aspects, Wound Repair Regen. 15 (1) (2007) 2–16, https://doi.org/10.1111/j.1524-475X.2006.00179.x.
[27] H.H. Sandstead, V.C. Lanier Jr., G.H. Shephard, D.D. Gillespie, Zinc and wound healing. Effects of zinc deficiency and zinc supplementation, Am. J. Clin. Nutr. 23 (5) (1970) 514–519, https://doi.org/10.1093/ajcn/23.5.514.
[28] M. Ramli, M.Z. Hussein, K. Yusoff, Preparation and characterization of an anti-inflammatory agent based on a zinc-layered hydroxide-salicylate nanohybrid and its effect on viability of Vero-3 cells, Int. J. Nanomed. 8 (2013) 297–306, https://doi.org/10.2147/IJN.S38858.
[29] K. Kawai, B.J. Larson, H. Ishise, A.L. Carre, S. Nishimoto, M. Longaker, H.P. Lorenz, Calcium-based nanoparticles accelerate skin wound healing, PLoS One 6 (11) (2011), e27106, https://doi.org/10.1371/journal.pone.0027106.
[30] T. Wang, Q. Gu, J. Zhao, J. Mei, M. Shao, Y. Pan, J. Zhang, H. Wu, Z. Zhang, F. Liu, Calcium alginate enhances wound healing by up-regulating the ratio of collagen types I/III in diabetic rats, Int. J. Clin. Exp. Pathol. 8 (6) (2015) 6636–6645.
[31] J. Niu, Z. Tang, H. Huang, J. Pei, H. Zhang, G. Yuan, W. Ding, Research on a Zn-Cu alloy as a biodegradable material for potential vascular stents application, Mater. Sci. Eng. C 69 (2016) 407–413, https://doi.org/10.1016/j.msec.2016.06.082.
[32] Z. Tang, H. Huang, J. Niu, L. Zhang, H. Zhang, J. Pei, J. Tan, G. Yuan, Design and characterizations of novel biodegradable Zn-Cu-Mg alloys for potential biodegradable implants, Mater. Des. 117 (2017) 84–94, https://doi.org/10.1016/j.matdes.2016.12.075.
[33] P. Li, W. Zhang, J. Dai, A.B. Xepapadeas, E. Schweizer, D. Alexander, L. Scheideler, C. Zhou, H. Zhang, G. Wan, J. Geis-Gerstorfer, Investigation of zinc-copper alloys as potential materials for craniomaxillofacial osteosynthesis implants, Mater. Sci. Eng. C 103 (2019) 109826, https://doi.org/10.1016/j.msec.2019.109826.
[34] A. Pola, M. Tocci, F.E. Goodwin, Review of microstructures and properties of zinc alloys, Metals 10 (2) (2020) 253.
[35] Z. Tang, J. Niu, H. Huang, H. Zhang, J. Pei, J. Ou, G. Yuan, Potential biodegradable Zn-Cu binary alloys developed for cardiovascular implant applications, J. Mech. Behav. Biomed. Mater. 72 (2017) 182–191, https://doi.org/10.1016/j.jmbbm.2017.05.013.
[36] Z.Z. Shi, X.X. Gao, H.J. Zhang, X.F. Liu, H.Y. Li, C. Zhou, Y.X. Yin, L.N. Wang, Design biodegradable Zn alloys: second phases and their significant influences on alloy properties, Bioactive Mater. 5 (2) (2020) 210–218, https://doi.org/10.1016/j.bioactmat.2020.02.010.
[37] Y. Zou, X. Chen, B. Chen, Effects of Ca concentration on degradation behavior of Zn-x Ca alloys in Hank's solution, Mater. Lett. 218 (2018) 193–196, https://doi.org/10.1016/j.matlet.2018.02.018.
[38] ASTM International, E8/E8M-16ae1, Standard Test Methods for Tension Testing of Metallic Materials, ASTM International, West Conshohocken, PA, 2016, https://doi.org/10.1520/E0008_E0008M-16AE01.
[39] ASTM International, E1382-97 Standard Test Methods for Determining Average Grain Size Using Semiautomatic and Automatic Image Analysis, ASTM

International, West Conshohocken, PA, 2015, https://doi.org/10.1520/E1382-97R15.
[40] ASTM International, E1245-03 Standard Practice for Determining the Inclusion or Second-phase Constituent Content of Metals by Automatic Image Analysis, ASTM International, West Conshohocken, PA, 2016, https://doi.org/10.1520/E1245-03R16.
[41] ASTM International, E9-19 Standard Test Methods of Compression Testing of Metallic Materials at Room Temperature, ASTM International, West Conshohocken, PA, 2004, https://doi.org/10.1520/E0009-19.
[42] ASTM International, E92-17 Standard Test Methods for Vickers Hardness and Knoop Hardness of Metallic Materials, ASTM International, West Conshohocken, PA, 2017, https://doi.org/10.1520/E0092-17.
[43] ASTM International, ASTM F3268-18a standard guide for in vitro degradation testing of absorbable metals, ASTM International, West Conshohocken, PA, 2018, https://doi.org/10.1520/F3268-18A.
[44] ASTM International, ASTM G102-89(2015)e1 Standard Practice for Calculation of Corrosion Rates and Related Information from Electrochemical Measurements, ASTM International, West Conshohocken, PA, 2015, https://doi.org/10.1520/G0102-89R15E01.
[45] H. Okamoto, Ca-Zn (Calcium-Zinc), J. Phase Equilibria Diffus. 34 (2) (2013) 171, https://doi.org/10.1007/s11669-012-0180-3, 171.
[46] H. Gong, K. Wang, R. Strich, J.G. Zhou, In vitro biodegradation behavior, mechanical properties, and cytotoxicity of biodegradable Zn–Mg alloy, J. Biomed. Mater. Res. B Appl. Biomater. 103 (8) (2015) 1632–1640, https://doi.org/10.1002/jbm.b.33341.
[47] J. Benavente, Electrochemical impedance spectroscopy as a tool for electrical and structural characterizations of membranes in contact with electrolyte solutions, in: A. Méndez-Vilas (Ed.), Recent Advances in Multidisciplinary Applied Physics, Elsevier Science Ltd, Oxford, 2005, pp. 463–471, https://doi.org/10.1016/B978-008044648-6.50074-4.
[48] K. Törne, M. Larsson, A. Norlin, J. Weissenrieder, Degradation of zinc in saline solutions, plasma, and whole blood. https://doi.org/10.1002/jbm.b.33458, 2016, 104, 6, 1141-1151.
[49] S. Champagne, E. Mostaed, F. Safizadeh, E. Ghali, M. Vedani, H. Hermawan, In Vitro degradation of absorbable zinc alloys in artificial urine, Materials 12 (2) (2019), https://doi.org/10.3390/ma12020295.
[50] Y. Meng, L. Liu, D. Zhang, C. Dong, Y. Yan, A.A. Volinsky, L.-N. Wang, Initial formation of corrosion products on pure zinc in saline solution, Bioactive Mater. 4 (2019) 87–96, https://doi.org/10.1016/j.bioactmat.2018.08.003.
[51] R. Kelly, J. Scully, D. Shoesmith, R. Buchheit, Electrochemical Techniques in Corrosion Science and Engineering, 2003, https://doi.org/10.1201/9780203909133.
[52] W.R. Osório, C. Brito, L.C. Peixoto, A. Garcia, Electrochemical behavior of Zn-rich Zn–Cu peritectic alloys affected by macrosegregation and microstructural array, Electrochim. Acta 76 (2012) 218–228, https://doi.org/10.1016/j.electacta.2012.04.122.
[53] K.B. Törne, A.Ö. Lic, J. Weissenrieder, F.A. Khan, Zn–Mg and zn–Ag degradation mechanism under biologically relevant conditions, Surface Innov. 6 (1–2) (2017) 81–92, https://doi.org/10.1680/jsuin.17.00053.
[54] M.B. Kannan, C. Moore, S. Saptarshi, S. Somasundaram, M. Rahuma, A.L. Lopata, Biocompatibility and biodegradation studies of a commercial zinc alloy for temporary mini-implant applications, Sci. Rep. 7 (1) (2017), https://doi.org/10.1038/s41598-017-15873-w.
[55] J.B. Jorcin, M.E. Orazem, N. Pébère, B. Tribollet, CPE analysis by local electrochemical impedance spectroscopy, Electrochim. Acta 51 (8) (2006) 1473–1479, https://doi.org/10.1016/j.electacta.2005.02.128.
[56] E. Mostaed, M. Sikora-Jasinska, J.W. Drelich, M. Vedani, Zinc-based alloys for degradable vascular stent applications, Acta Biomater. 71 (2018) 1–23, https://doi.org/10.1016/j.actbio.2018.03.005.
[57] J. Lin, X. Tong, Z. Shi, D. Zhang, L. Zhang, K. Wang, A. Wei, L. Jin, J. Lin, Y. Li, C. Wen, A biodegradable Zn-1Cu-0.1Ti alloy with antibacterial properties for orthopedic applications, Acta Biomater. 106 (2020) 410–427, https://doi.org/10.1016/j.actbio.2020.02.017.
[58] M. Gholami, M. Mhaede, F. Pastorek, I. Altenberger, B. Hadzima, M. Wollmann, L. Wagner, Corrosion behavior and mechanical properties of ultrafine-grained pure copper with potential as a biomaterial, Adv. Eng. Mater. 18 (4) (2016) 615–623, https://doi.org/10.1002/adem.201500269.
[59] A. Fattah-alhosseini, O. Imantalab, S. Vafaeian, G. Ansari, Corrosion behavior of pure copper surrounded by Hank's physiological electrolyte at 310 K (37 °C) as a potential biomaterial for contraception: an analogy drawn between micro- and nano-grained copper, J. Mater. Eng. Perform. 26 (8) (2017) 3739–3749, https://doi.org/10.1007/s11665-017-2825-1.
[60] N. Mora, E. Cano, E.M. Mora, J.M. Bastidas, Influence of pH and oxygen on copper corrosion in simulated uterine fluid, Biomaterials 23 (3) (2002) 667–671, https://doi.org/10.1016/S0142-9612(01)00154-5.
[61] F. Wang, Z. Liu, D. Qiu, J.A. Taylor, M.A. Easton, M.-X. Zhang, Revisiting the role of peritectics in grain refinement of Al alloys, Acta Mater. 61 (1) (2013) 360–370, https://doi.org/10.1016/j.actamat.2012.09.075.
[62] Z. Liu, D. Qiu, F. Wang, J.A. Taylor, M. Zhang, Crystallography of grain refinement in cast zinc-copper alloys, J. Appl. Crystallogr. 48 (3) (2015) 890–900, https://doi.org/10.1107/S1600576715008936.
[63] W.D. Callister, D.G. Rethwisch, Materials Science and Engineering: an Introduction, eighth ed., 2009.
[64] J. Pinc, J. Čapek, J. Kubásek, P. Veřtát, K. Hosová, Microstructure and mechanical properties of the potentially biodegradable ternary system Zn-Mg0.8-Ca0.2, Procedia Struct. Integr. 23 (2019) 21–26, https://doi.org/10.1016/j.prostr.2020.01.057.
[65] X. Liu, J. Sun, K. Qiu, Y. Yang, Z. Pu, L. Li, Y. Zheng, Effects of alloying elements (Ca and Sr) on microstructure, mechanical property and in vitro corrosion behavior of biodegradable Zn–1.5Mg alloy, J. Alloys Compd. 664 (2016) 444–452, https://doi.org/10.1016/j.jallcom.2015.10.116.
[66] L.Q. Wang, S.N. Sun, Y.P. Ren, G.W. Qin, Effect of Mg, Ca addition on microstructure and properties of biodegradable Zn alloy, Dongbei Daxue Xuebao/J. Northeastern Univ. 39 (1) (2018) 35–39, https://doi.org/10.12068/j.issn.1005-3026.2018.01.008.
[67] Z.Z. Shi, J. Yu, X.F. Liu, H.J. Zhang, D.W. Zhang, Y.X. Yin, L.N. Wang, Effects of Ag, Cu or Ca addition on microstructure and comprehensive properties of biodegradable Zn-0.8Mn alloy, Mater. Sci. Eng. C 99 (2019) 969–978, https://doi.org/10.1016/j.msec.2019.02.044.
[68] M.Ş. Turhal, T. Savaşkan, Relationships between secondary dendrite arm spacing and mechanical properties of Zn-40Al-Cu alloys, J. Mater. Sci. 38 (12) (2003) 2639–2646, https://doi.org/10.1023/A:1024434602540.
[69] W.R. Osório, A. Garcia, Modeling dendritic structure and mechanical properties of Zn–Al alloys as a function of solidification conditions, Mater. Sci. Eng., A 325 (1) (2002) 103–111, https://doi.org/10.1016/S0921-5093(01)01455-1.
[70] R. Yue, H. Huang, G. Ke, H. Zhang, J. Pei, G. Xue, G. Yuan, Microstructure, mechanical properties and in vitro degradation behavior of novel Zn-Cu-Fe alloys, Mater. Char. 134 (2017) 114–122, https://doi.org/10.1016/j.matchar.2017.10.015.
[71] Z.Z. Shi, J. Yu, X.F. Liu, L.N. Wang, Fabrication and characterization of novel biodegradable Zn-Mn-Cu alloys, J. Mater. Sci. Technol. 34 (6) (2018) 1008–1015, https://doi.org/10.1016/j.jmst.2017.11.026.
[72] Z.Z. Shi, H.Y. Li, J.Y. Xu, X.X. Gao, X.F. Liu, Microstructure evolution of a high-strength low-alloy Zn–Mn–Ca alloy through casting, hot extrusion and warm caliber rolling, Mater. Sci. Eng., A 771 (2020) 138626, https://doi.org/10.1016/j.msea.2019.138626.
[73] M.S. Dambatta, S. Izman, D. Kurniawan, S. Farahany, B. Yahaya, H. Hermawan, Influence of thermal treatment on microstructure, mechanical and degradation properties of Zn-3Mg alloy as potential biodegradable implant material, Mater. Des. 85 (2015) 431–437, https://doi.org/10.1016/j.matdes.2015.06.181.
[74] X. Liu, J. Sun, F. Zhou, Y. Yang, R. Chang, K. Qiu, Z. Pu, L. Li, Y. Zheng, Micro-alloying with Mn in Zn–Mg alloy for future biodegradable metals application, Mater. Des. 94 (2016) 95–104, https://doi.org/10.1016/j.matdes.2015.12.128.
[75] S. Qu, J. Xia, J. Yan, H. Wu, H. Wang, Y. Yi, X. Zhang, S. Zhang, C. Zhao, Y. Chen, In vivo and in vitro assessment of the biocompatibility and degradation of high-purity Mg anastomotic staples, J. Biomater. Appl. 31 (8) (2017) 1203–1214, https://doi.org/10.1177/0885328217692948.
[76] H. Wu, C. Zhao, J. Ni, S. Zhang, J. Liu, J. Yan, Y. Chen, X. Zhang, Research of a novel biodegradable surgical staple made of high purity magnesium, Bioactive Mater. 1 (2) (2016) 122–126, https://doi.org/10.1016/j.bioactmat.2016.09.005.
[77] H. Amano, K. Hanada, A. Hinoki, T. Tainaka, C. Shirota, W. Sumida, K. Yokota, N. Murase, K. Oshima, K. Chiba, Y. Tanaka, H. Uchida, Biodegradable surgical staple composed of magnesium alloy, Sci. Rep. 9 (1) (2019) 14671, https://doi.org/10.1038/s41598-019-51123-x.
[78] H. Amano, K. Miyake, A. Hinoki, K. Yokota, F. Kinoshita, A. Nakazawa, Y. Tanaka, Y. Seto, H. Uchida, Novel zinc alloys for biodegradable surgical staples, World J. Clin. Cases 8 (3) (2020) 504.
[79] J.M. Seitz, D. Utermöhlen, E. Wulf, C. Klose, F.W. Bach, The manufacture of resorbable suture material from magnesium – drawing and stranding of thin wires, Adv. Eng. Mater. 13 (2011) 1087–1095, https://doi.org/10.1002/adem.201100152.
[80] F. Witte, N. Hort, C. Vogt, S. Cohen, K.U. Kainer, R. Willumeit, F. Feyerabend, Degradable biomaterials based on magnesium corrosion, Curr. Opin. Solid State Mater. Sci. 12 (5) (2008) 63–72, https://doi.org/10.1016/j.cossms.2009.04.001.
[81] M.S. Dambatta, S. Izman, D. Kurniawan, H. Hermawan, Processing of Zn-3Mg alloy by equal channel angular pressing for biodegradable metal implants, J. King Saud Univ. Sci. 29 (4) (2017) 455–461, https://doi.org/10.1016/j.jksus.2017.07.008.
[82] D.A. Jones, Principles and Prevention of Corrosion, second ed., Prentice Hall, Upper Saddle River, NJ, 1996.
[83] L. Nyikos, T. Pajkossy, Fractal dimension and fractional power frequency-dependent impedance of blocking electrodes, Electrochim. Acta 30 (11) (1985) 1533–1540, https://doi.org/10.1016/0013-4686(85)80016-5.
[84] H.K. Song, H.Y. Hwang, K.H. Lee, L. Dao, Effect of pore size distribution on the frequency dispersion of porous electrodes, Electrochim. Acta 45 (2000) 2241–2257, https://doi.org/10.1016/S0013-4686(99)00436-3.
[85] T.M. Nahir, Impedance Spectroscopy: theory, experiment, and applications, J. Am. Chem. Soc. 127 (35) (2005) 12431, https://doi.org/10.1021/ja059742o, 12431.